

Performance Analysis for Near-Field ISAC: A Holographic MIMO Design

Boqun Zhao, *Graduate Student Member, IEEE*, Chongjun Ouyang,
Xingqi Zhang, *Member, IEEE*, and Yuanwei Liu, *Fellow, IEEE*

Abstract—A near-field holographic multiple-input multiple-output (MIMO) based integrated sensing and communications (ISAC) framework is proposed for both downlink and uplink scenarios, where spherical wave-based model is considered to capture the characteristics of the near field. The coupling effect introduced by the densely spaced antennas of the holographic MIMO are characterized by spatially correlated Rayleigh fading. Based on the proposed framework, by considering both instantaneous channel state information (CSI) and statistical CSI, closed-form expressions are derived for sensing rates (SRs), communication rates (CRs), and outage probabilities under different ISAC designs. Further insights are gained by examining high signal-to-noise ratio slopes and diversity orders. Specifically, 1) for the downlink case, a sensing-centric (S-C) design and a communications-centric (C-C) design are investigated based on different beamforming strategies, and a Pareto optimal design is proposed to characterize the attainable SR-CR region; and 2) for the uplink case, the S-C design and the C-C design are distinguished by the interference cancellation order of the communication signal and the sensing signal, and the rate region is obtained through a time-sharing strategy. Numerical results reveal that the proposed ISAC system achieves more extensive rate regions than the conventional frequency-division sensing and communications system, highlighting its superior performance.

Index Terms—Holographic multiple-input multiple-output, integrated sensing and communications (ISAC), near field, performance analysis, spatially correlated channels.

I. INTRODUCTION

The concept of Integrated Sensing and Communications (ISAC) has attracted substantial attention from both academia and industry, due to its potential contributions to the development of sixth-generation (6G) and future wireless networks [1]. A distinctive feature that sets ISAC apart is its ability to share the same hardware, power, frequency, and time resources for both communication and sensing purposes. This stands in contrast to the conventional approach of Frequency-Division Sensing and Communications (FDSAC), which necessitates isolated infrastructures and frequency ranges for the two functions. Consequently, compared to FDSAC, ISAC is anticipated to be more effective in terms of spectrum utilization, energy consumption, and hardware requirements [2], [3].

Recently, the emergence of the concept of holographic multiple-input multiple-output (MIMO), inspired by the

promising beamforming gains of massive MIMO with its large-scale aperture array, has gained prominence. Holographic MIMO is characterized by a larger and denser array, containing a substantial quantity of antennas spaced at intervals smaller than half of the wavelength [4]–[6]. This technology has been proposed to significantly enhance the capabilities of wireless transmissions, especially considering its potential integration into 6G networks [4]. Leveraging this advantage, recent work, such as [7], [8], has applied holographic MIMO to ISAC, which we refer to as holographic ISAC (HISAC) for simplicity. This innovation has demonstrated the potential to enhance the performance of sensing and communications (S&C) through a well-designed beamforming strategy.

A. Prior Works

The transition from large-scale aperture arrays in massive MIMO to extremely large aperture arrays in holographic MIMO signifies more than a mere quantitative increase in array aperture; it represents a qualitative paradigm shift from traditional *far-field* ISAC to *near-field* ISAC [9]. In the far-field region, electromagnetic (EM) waves exhibit distinct propagation characteristics compared to the near-field region. While planar waves effectively approximate the far-field EM field, the near-field EM field demands precise modeling using spherical waves [10]. Therefore, the conventional planar wave model, prevalent in previous studies investigating ISAC performance within the far-field region (e.g., [11]–[14]), loses validity in the near-field region. As a result, a reassessment of ISAC system performance from a near-field perspective becomes imperative.

While there have been several studies exploring near-field ISAC, this field is still in its infancy. Zhang *et al.* provided concise yet comprehensive overviews of HISAC's hardware structure and working principles, identifying challenges and outlining future research opportunities for implementing HISAC networks [7]. Similarly, Cong *et al.* presented insights into how the near field influences ISAC and explored the potential of near-field ISAC [15]. Additionally, the works in [16]–[18] and [8] primarily focused on aspects related to waveform or beamforming design for near-field ISAC and HISAC, respectively.

In contrast, there is a limited body of works analyzing the fundamental performance limits of near-field ISAC, as demonstrated by [19]. However, existing works only discussed *line-of-sight communication channels*, which are not practical in real-world scenarios due to the presence of scatterers [19]. From an information-theoretic perspective, the performance limits of S&C can be evaluated by the sensing rate (SR) and communication rate (CR), respectively [2], [20]. SR measures

B. Zhao and X. Zhang are with the Department of Electrical and Computer Engineering, University of Alberta, Edmonton, T6G 2H5, Canada (email: {boqun1, xingqi.zhang}@ualberta.ca).

C. Ouyang is with the School of Electrical and Electronic Engineering, University College Dublin, Dublin, D04 V1W8, Ireland (e-mail: chongjun.ouyang@ucd.ie).

Y. Liu is with the School of Electronic Engineering and Computer Science, Queen Mary University of London, London, E1 4NS, U.K. (email: yuanwei.liu@qmul.ac.uk).

the system's capability to estimate environmental information via sensing processes, while CR measures the system's capacity for data transmission through communication processes [20]. A comprehensive analysis of these two metrics provides valuable insights into the overall performance and effectiveness of ISAC in seamlessly integrating S&C functions. As of now, the performance of near-field HISAC under scattering in terms of CR and SR has not been fully understood.

B. Motivations and Contributions

This article aims to fill the existing knowledge gap by undertaking a comprehensive analysis of the SR and CR in a near-field HISAC system. As an improvement of previous efforts in [19], our work incorporates *the influence of scattering* when modeling *the communication channel*. The distinctive feature of holographic MIMO lies in the deployment of an extremely large aperture array with sub-half-wavelength spacing, inducing spatial correlation among the antenna elements across the entire array. Consequently, the channel fading within holographic MIMO exhibits inherent spatial correlation, discouraging the use of the more simplistic independent and identically distributed (i.i.d.) Rayleigh fading [6]. Moreover, unlike the planar wave approximation employed in the far field, the more intricate spherical wave must be considered in the near-field region.

Owing to these unique characteristics associated with holographic MIMO, analyzing the S&C performance of near-field HISAC proves to be a challenging task. In an effort to address these challenges, this article endeavors to derive closed-form expressions for SR and CR, thereby offering insights into the S&C performance of HISAC. The main contributions of this article can be summarized as follows:

- We propose a near-field HISAC framework tailored for both downlink and uplink scenarios, where the dual-functional S&C (DFSAC) base station (BS) is equipped with a holographic uniform planar array (UPA). In this framework, we employ a correlated Rayleigh fading model to characterize the communication link. Specifically, we leverage an approximated Fourier plane-wave series expansion to effectively capture the properties associated with spherical-wave propagations [21]. Meanwhile, we utilize a spherical wave-based free-space deterministic model to describe the sensing link.
- By considering different types of channel state information (CSI) available to the BS, namely instantaneous CSI (I-CSI) and statistical CSI (S-CSI), we derive closed-form expressions for SRs, CRs, and outage probabilities (OPs) based on the proposed channel models and various ISAC designs. For the downlink scenario, we investigate sensing-centric (S-C) and communications-centric (C-C) designs, aiming to design DFSAC beamforming strategies that maximize SR and CR, respectively. The SR-CR region is further characterized through a Pareto optimal beamforming design. In the uplink case, we consider S-C and C-C designs, each employing distinct interference cancellation orders for S&C signals at the BS. The rate region is obtained through the time-sharing strategy between these two designs.

- We present numerical results to demonstrate that i) near-field HISAC achieves higher SRs and CRs than FDSAC in both downlink and uplink scenarios; ii) near-field HISAC yields more degrees of freedom (DoFs) than FDSAC; and iii) the achievable SR-CR rate regions of FDSAC are entirely encompassed within the rate regions of HISAC. These findings emphasize the superiority of HISAC over FDSAC in the near field.

C. Organization and Notations

The remainder of this article is organized as follows. Section II presents the conceptual framework of the near-field HISAC, including both S&C models. Then, Sections III and IV delve into the analysis of downlink and uplink S&C performance, respectively, elucidating the outcomes for both I-CSI and S-CSI. Section V provides numerical results to validate the accuracy of the derived theoretical insights. Finally, Section VI concludes the article.

Notations: Throughout this paper, scalars, vectors, and matrices are denoted by non-bold, bold lower-case, and bold upper-case letters, respectively. For the matrix \mathbf{A} , $[\mathbf{A}]_{i,j}$, \mathbf{A}^T , \mathbf{A}^* , \mathbf{A}^H , and $\text{rank}(\mathbf{A})$ denote the (i,j) th entry, transpose, conjugate, transpose conjugate, and rank of \mathbf{A} , respectively. For the square matrix \mathbf{B} , $\mathbf{B}^{\frac{1}{2}}$, \mathbf{B}^{-1} , $\text{tr}(\mathbf{B})$, and $\det(\mathbf{B})$ denote the principal square root, inverse, trace, and determinant of \mathbf{B} , respectively. The notation $[\mathbf{a}]_i$ denotes the i th entry of vector \mathbf{a} , and $\text{diag}\{\mathbf{a}\}$ returns a diagonal matrix whose diagonal elements are entries of \mathbf{a} . The notations $|a|$, $\|\mathbf{a}\|$, and $\|\mathbf{A}\|_F$ denote the magnitude, norm, and Frobenius norm of scalar a , vector \mathbf{a} , and matrix \mathbf{A} , respectively. The identity matrix, zero matrix, and all-one matrix are represented by \mathbf{I} , $\mathbf{0}$, and $\mathbf{1}$, respectively. The matrix inequalities $\mathbf{A} \succeq \mathbf{0}$ and $\mathbf{A} \succ \mathbf{0}$ imply that \mathbf{A} is positive semi-definite and positive definite, respectively. The sets \mathbb{Z} , \mathbb{R} , and \mathbb{C} stand for the integer, real, and complex spaces, respectively, and notation $\mathbb{E}\{\cdot\}$ represents mathematical expectation. The mutual information between random variables X and Y conditioned on Z is shown by $I(X;Y|Z)$, and \otimes denotes the Kronecker product. The modulus operator and the floor function are represented by $\text{mod}(\cdot, \cdot)$ and $\lfloor \cdot \rfloor$, respectively. Finally, $\mathcal{CN}(\boldsymbol{\mu}, \mathbf{X})$ is used to denote the circularly-symmetric complex Gaussian distribution with mean $\boldsymbol{\mu}$ and covariance matrix \mathbf{X} .

II. SYSTEM MODEL

Consider a downlink/uplink near-field HISAC system as depicted in Fig. 1(a), where a DFSAC BS is equipped with a holographic UPA comprising N antennas. The BS aims to serve a single-antenna communication user (CU) while simultaneously sensing a single target. The sensing setup at the BS is monostatic, and both the CU and the target are positioned within the near-field region. As shown in Fig. 1(b), we assume that the UPA is deployed on the x - y plane with $N = N_x N_y$, where N_x and N_y denote the number of antennas along the x -axis and y -axis, respectively. The inter-element distance is denoted as d ($d < \lambda/2$), where λ denotes the wavelength. Hence, the UPA has the size of $L_x \times L_y$ with $L_x = N_x d$ and $L_y = N_y d$, and centered at $\mathbf{c} = [L_x/2, L_y/2, 0]^T$. By indexing

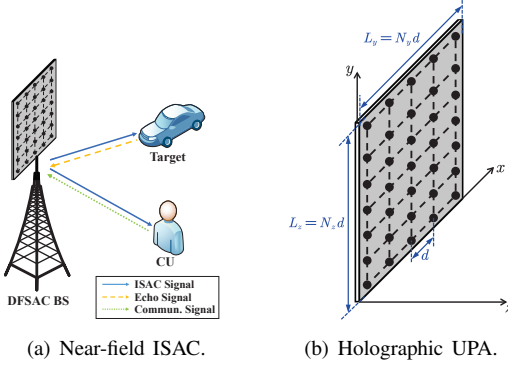


Fig. 1: Illustration of near-field holographic ISAC.

the antennas row-by-row, the location of the n th antenna for $n = 1, \dots, N$ can be characterized as follows:

$$\begin{aligned} \mathbf{p}_n &= [p_{n,x}, p_{n,y}, p_{n,z}]^T \\ &= [\text{mod}(n-1, N_x)d, [(n-1)/N_y]d, 0]^T. \end{aligned} \quad (1)$$

A. Downlink Signal Model

We commence by considering the downlink ISAC scenario, where the DFSAC signals sent by the BS are used to deliver data information to the CU and sense the environmental information at the same time. Let $\mathbf{X} = [\mathbf{x}_1 \dots \mathbf{x}_L] \in \mathbb{C}^{N \times L}$ be a DFSAC signal sent from the BS, where L denotes the length of the communication frame/sensing pulse. From a sensing perspective, $\mathbf{x}_\ell \in \mathbb{C}^{N \times 1}$ denotes the sensing snapshot transmitted during the ℓ th time slot for $\ell = 1, \dots, L$. From a communication perspective, \mathbf{x}_ℓ corresponds to the ℓ th data symbol vector. Under the proposed HISAC framework, the downlink ISAC signal \mathbf{X} is given by

$$\mathbf{X} = \sqrt{p} \mathbf{w} \mathbf{s}^H, \quad (2)$$

where $\mathbf{w} \in \mathbb{C}^{N \times 1}$ represents the normalized beamforming vector with $\|\mathbf{w}\|^2 = 1$, p is the power budget, and $\mathbf{s} = [s_1 \dots s_L]^H \in \mathbb{C}^{L \times 1}$ denotes the unit-power data stream intended for the CU with $L^{-1}\|\mathbf{s}\|^2 = 1$.

1) *Sensing Model*: We assume that the target is located in the near-field region with its location given by $\mathbf{r}_s = [r_{s,x}, r_{s,y}, r_{s,z}]^T$. Since the planar wave model is no longer valid within the near field, the EM link should be accurately modeled based on the spherical wave assumption. Let $\mathbf{h}_s \in \mathbb{C}^{N \times 1}$ denote the sensing link between the BS and the target. Then the channel coefficient between the n th antenna and the target is given by [9], [22]

$$[\mathbf{h}_s]_n = \frac{\sqrt{\alpha_0}}{\sqrt{4\pi r_s^2}} e^{-jk_0 \|\mathbf{r}_s - \mathbf{p}_n\|}, \quad (3)$$

for $n = 1, \dots, N$, where $r_s = \|\mathbf{r}_s - \mathbf{c}\|$ is the propagation distance, $k_0 = \frac{2\pi}{\lambda}$ is the wavenumber, and α_0 denotes the channel power at the reference distance 1 m.

When transmitting the DFSAC signal matrix \mathbf{X} for target sensing, the received reflected echo signal at the BS can be written as follows:

$$\mathbf{Y}_s = \mathbf{G} \mathbf{X} + \mathbf{N}_s, \quad (4)$$

where $\mathbf{G} \in \mathbb{C}^{N \times N}$ denotes the target response matrix, and $\mathbf{N}_s \in \mathbb{C}^{N \times L}$ denotes the additive white Gaussian noise

(AWGN) matrix with each entry having mean zero and variance σ_s^2 . Furthermore, the target response matrix can be modeled by the round-trip channel as follows: [19], [23]

$$\mathbf{G} = \beta \mathbf{h}_s \mathbf{h}_s^H, \quad (5)$$

where $\beta \sim \mathcal{CN}(0, \alpha_s)$ denotes the complex amplitude of the target with the average strength of α_s . Substituting (2) and (5) into (4) gives

$$\mathbf{Y}_s = \sqrt{p} \beta \mathbf{h}_s \mathbf{h}_s^H \mathbf{w} \mathbf{s}^H + \mathbf{N}_s. \quad (6)$$

We assume that the location of the target is perfectly tracked and focus on the estimation of the reflection coefficient β . This sensing task aims to extract environmental information contained within β from the echo signal \mathbf{Y}_s , given the foreknowledge of the DFSAC signal \mathbf{X} . The information-theoretic limit for this sensing task can be quantified by the sensing mutual information (MI) that characterizes the MI between \mathbf{Y}_s and β conditioned on \mathbf{X} [20]. On this basis, we employ the SR as the metric for sensing performance evaluation, which is defined as the sensing MI per unit time [20], [23]. Assuming that each DFSAC symbol lasts 1 unit time, the SR is written as follows:

$$\mathcal{R}_{d,s} = L^{-1} I(\mathbf{Y}_s; \beta | \mathbf{X}). \quad (7)$$

In particular, $\mathcal{R}_{d,s}$ can be calculated in the following form.

Lemma 1. Given \mathbf{w} , the SR can be expressed as follows:

$$\mathcal{R}_{d,s} = L^{-1} \log_2(1 + p \sigma_s^{-2} L \alpha_s \|\mathbf{h}_s\|^2 |\mathbf{w}^H \mathbf{h}_s|^2). \quad (8)$$

Proof: Please refer to Appendix A for more details. ■

2) *Communication Model*: We assume that the CU is also situated in the near-field region, with its position denoted by $\mathbf{r}_c = [r_{c,x}, r_{c,y}, r_{c,z}]^T$. Due to the sub-half-wavelength antenna spacing in the holographic array and the presence of scatterers, spatial correlation for the small-scale fading between antennas becomes significant. Therefore, we model the communication channel response $\mathbf{h}_c \in \mathbb{C}^{N \times 1}$ as a correlated Rayleigh-distributed vector, i.e., $\mathbf{h}_c \sim \mathcal{CN}(\mathbf{0}, \mathbf{R})$, where $\mathbf{R} = \mathbb{E}\{\mathbf{h}_c \mathbf{h}_c^H\} \succeq \mathbf{0}$ is the correlation matrix.

Moreover, conventional stochastic models derived under the far-field assumption, i.e., planar wave approximation over the array, become inadequate in the near-field region. To address these issues, we employ a correlation model based on the Fourier plane-wave series expansion of an EM random channel [21]. This model effectively captures the spatial correlation effects and aligns with the physics of spherical wave propagation under a near-field scattering environment. Following the methodology in [21], the spatial impulse response $[\mathbf{h}_c]_n$ can be derived based on a four-dimensional (4D) Fourier plane-wave representation, given by

$$[\mathbf{h}_c]_n = \frac{1}{4\pi^2} \iiint_{\mathcal{D}} \int_{\mathcal{D}} a_c(k_x, k_y, \mathbf{r}_c) H_a(k_x, k_y, \kappa_x, \kappa_y) \times a_b(\kappa_x, \kappa_y, \mathbf{p}_n) dk_x dk_y d\kappa_x d\kappa_y, \quad (9)$$

where $\boldsymbol{\kappa} = [\kappa_x, \kappa_y, \kappa_z]^T$ with $\kappa_z = (k_0^2 - \kappa_x^2 - \kappa_y^2)^{\frac{1}{2}}$, $\mathbf{k} = [k_x, k_y, k_z]^T$ with $k_z = (k_0^2 - k_x^2 - k_y^2)^{\frac{1}{2}}$,

$$a_b(\kappa_x, \kappa_y, \mathbf{p}_n) = e^{-jk_0(\kappa_x p_{n,x} + \kappa_y p_{n,y} + \kappa_z p_{n,z})}, \quad (10)$$

$$a_c(k_x, k_y, \mathbf{r}_c) = e^{jk_0(k_x r_{c,x} + k_y r_{c,y} + k_z r_{c,z})} \quad (11)$$

denote the transmit and receive responses at \mathbf{p}_n and \mathbf{r}_c , respectively, and the integration region \mathcal{D} is given by $\mathcal{D} = \{(x, y) \in \mathbb{R}^2 | x^2 + y^2 \leq k_0^2\}$. Besides, $H_a(k_x, k_y, \kappa_x, \kappa_y)$ in (9)

is referred to as the angular or wavenumber response between the transmit propagation direction $\frac{\mathbf{k}}{\|\mathbf{k}\|}$ of the BS and the receive propagation direction $\frac{\mathbf{k}}{\|\mathbf{k}\|}$ of the CU, which is complex Gaussian distributed with mean zero and variance determined by the scattering environment and the array geometry [21].

According to [6], [21], the channel description in (9) can be discretized via the Karhunen-Loève expansion as follows:

$$\mathbf{h}_c = \sqrt{N} \sum_{(m_x, m_y) \in \mathcal{E}} H(m_x, m_y) \mathbf{a}(m_x, m_y), \quad (12)$$

where $[\mathbf{a}(m_x, m_y)]_n = \frac{1}{\sqrt{N}} a_b(\frac{2\pi m_x}{L_x}, \frac{2\pi m_y}{L_y}, \mathbf{p}_n) e^{jk_0 r_{c,z}}$ for $n = 1, \dots, N$, $\mathcal{E} = \{(m_x, m_y) \in \mathbb{Z}^2 : (\frac{m_x \lambda}{L_x})^2 + (\frac{m_y \lambda}{L_y})^2 < 1\}$, and the set $\{H(m_x, m_y) \sim \mathcal{CN}(0, \sigma^2(m_x, m_y))\}_{(m_x, m_y) \in \mathcal{E}}$ stores $|\mathcal{E}| \triangleq n$ statistically independent complex Gaussian variables each with variance $\sigma^2(m_x, m_y)$ determined by [6, Eq. (70)]. As a result, \mathbf{h}_c can be reexpressed as follows: [21]

$$\mathbf{h}_c = \mathbf{U} \mathbf{\Sigma}^{\frac{1}{2}} \bar{\mathbf{h}}, \quad (13)$$

where $\bar{\mathbf{h}} \sim \mathcal{CN}(\mathbf{0}, \mathbf{I})$ contains n independently distributed Gaussian variables, $\mathbf{\Sigma} \in \mathbb{C}^{n \times n}$ is a diagonal matrix whose diagonal elements are $\{N\sigma^2(m_x, m_y)\}_{(m_x, m_y) \in \mathcal{E}}$, and $\mathbf{U} \in \mathbb{C}^{N \times n}$ is a deterministic semi-unitary matrix collecting the n vectors $\{\mathbf{a}(m_x, m_y)\}_{(m_x, m_y) \in \mathcal{E}}$ with $\mathbf{U}^H \mathbf{U} = \mathbf{I}$. Based on (13), the correlation matrix \mathbf{R} can be written as follows:

$$\mathbf{R} = \mathbb{E} \{\mathbf{h}_c \mathbf{h}_c^H\} = \mathbf{U} \mathbf{\Sigma} \mathbf{U}^H. \quad (14)$$

Note that (14) can be regarded as the eigendecomposition (ED) of \mathbf{R} with $\text{rank}(\mathbf{R}) = n$ and its n positive eigenvalues stored in $\{N\sigma^2(m_x, m_y)\}_{(m_x, m_y) \in \mathcal{E}} \triangleq \{\lambda_1 \geq \dots \geq \lambda_n > 0\}$.

The received downlink signal at the CU is given by

$$\mathbf{y}_c = \mathbf{h}_c^H \mathbf{X} + \mathbf{n}_c^H = \sqrt{p} \mathbf{h}_c^H \mathbf{w} \mathbf{s}^H + \mathbf{n}_c^H, \quad (15)$$

where $\mathbf{n}_c \in \mathbb{C}^{L \times 1}$ denotes the AWGN vector with each entry having mean zero and variance σ_c^2 . Consequently, the downlink CR can be written as follows:

$$\bar{\mathcal{R}}_{d,c} = \log_2(1 + p/\sigma_c^2 |\mathbf{w}^H \mathbf{h}_c|^2). \quad (16)$$

Downlink Beamforming Design: By observing (8) and (16), one can find that both the SR and CR are influenced by the beamforming vector \mathbf{w} . However, finding an optimal \mathbf{w} that can simultaneously maximize both the CR and SR poses a challenging task. In light of this, we will propose three beamforming designs for the downlink HISAC in Section III. The first is named the *C-C (communications-centric) design*, aiming to maximize the CR, while the second one is termed the *S-C (sensing-centric) design*, focusing on maximizing the SR. Finally, we propose a *Pareto optimal design* to characterize the Pareto boundary of the SR-CR region.

B. Uplink Signal Model

For the uplink case, the DFSAC BS aims to extract environmental information from the reflected sensing echoes while simultaneously detecting the data symbols sent by the CU. The sensing and communication signals are assumed to be perfectly synchronized at the BS by using properly designed synchronization sequences. As a result, the BS observes the following superposed S&C signal:

$$\mathbf{Y}_u = \sqrt{p_c} \mathbf{h}_c \mathbf{s}_c^H + \sqrt{p_s} \mathbf{G} \mathbf{w} \mathbf{s}_s^H + \mathbf{N}_u, \quad (17)$$

where p_c is the communication power budget, $\mathbf{s}_c = [s_{c,1} \dots s_{c,L}]^H \in \mathbb{C}^{L \times 1}$ denotes the message sent by the CU subject to $\mathbb{E}\{\mathbf{s}_c \mathbf{s}_c^H\} = \mathbf{I}$, p_s is the sensing power budget, $\mathbf{s}_s = [s_{s,1} \dots s_{s,L}]^H \in \mathbb{C}^{L \times 1}$ denotes the sensing pulse subject to $L^{-1} \|\mathbf{s}_s\|^2 = 1$, and $\mathbf{N} \in \mathbb{C}^{N \times L}$ is the AWGN matrix with each entry having mean zero and variance σ_u^2 .

Uplink Interference Cancellation Design: To address the inter-functionality interference (IFI) between the S&C signals, the method of successive interference cancellation (SIC) with two different interference cancellation orders can be employed [20]. The first is named the *S-C SIC*, where the BS first detects the communication signal \mathbf{s}_c by treating the sensing signal as interference, and then $\sqrt{p_c} \mathbf{h}_c \mathbf{s}_c^H$ is subtracted from the superposed signal \mathbf{Y}_u , with the remaining part utilized for sensing the target response. The second one is termed the *C-C SIC*, where the BS first senses the target response \mathbf{G} by treating the communication signal as interference, and then $\sqrt{p_s} \mathbf{G} \mathbf{w} \mathbf{s}_s^H$ is subtracted from \mathbf{Y}_u , with the rest part used for detecting the communication signal. Clearly, *the first SIC order yields better communication performance, while the second one yields better sensing performance*, which will be further discussed in Section IV.

In the context of the near-field HISAC framework, our aim is to assess its S&C performance in both downlink and uplink scenarios. In the following pages, we will integrate two distinct CSI assumptions into our analyses: *I-CSI (instantaneous CSI)* and *S-CSI (statistical CSI)*. In the I-CSI case, the BS is assumed to possess perfect knowledge of \mathbf{h}_c , while in the S-CSI case, the BS only has information about the distribution of \mathbf{h}_c and its correlation matrix \mathbf{R} .

III. DOWNLINK PERFORMANCE ANALYSIS

In this section, we analyze the S&C performance of the downlink near-field HISAC. Specifically, the communication performance is evaluated using the ergodic CR (ECR) and OP, whereas the sensing performance is evaluated through the SR.

A. Instantaneous CSI

1) Sensing-Centric Design: Under the S-C design, the beamforming vector \mathbf{w} is set to maximize the downlink SR, and the optimal beamforming vector satisfies

$$\mathbf{w} = \arg\max_{\|\mathbf{w}\|^2=1} \mathcal{R}_{d,s} \quad (18)$$

$$= \arg\max_{\|\mathbf{w}\|^2=1} |\mathbf{w}^H \mathbf{h}_s|^2 = \mathbf{h}_s \|\mathbf{h}_s\|^{-1}. \quad (19)$$

By substituting $\mathbf{w} = \mathbf{h}_s \|\mathbf{h}_s\|^{-1}$ into (8), we write the SR as follows:

$$\mathcal{R}_{d,s}^s = L^{-1} \log_2(1 + p \sigma_s^{-2} L \alpha_s \|\mathbf{h}_s\|^4). \quad (20)$$

The following theorem provides a closed-form expression for $\mathcal{R}_{d,s}^s$ as well as its high-SNR approximation.

Theorem 1. In the S-C design, the downlink SR is given by

$$\mathcal{R}_{d,s}^s = L^{-1} \log_2 \left(1 + \frac{p L \alpha_s \alpha_0^2 N^2}{16 \pi^2 \sigma_s^2 r_s^4} \right). \quad (21)$$

When $p \rightarrow \infty$, the SR satisfies

$$\mathcal{R}_{d,s}^s \approx L^{-1} \log_2 p + L^{-1} \log_2 \left(\frac{L \alpha_s \alpha_0^2 N^2}{16 \pi^2 \sigma_s^2 r_s^4} \right). \quad (22)$$

Proof: Based on (3), we have $\|\mathbf{h}_s\|^4 = \frac{\alpha_0^2 N^2}{16\pi^2 r_s^4}$, which yields (21). Let $p \rightarrow \infty$ and apply the fact of $\lim_{x \rightarrow \infty} \frac{\log_2(1+x)}{\log_2 x} = 1$ to (21), we can obtain (22). ■

Remark 1. The results in Theorem 1 suggest that the high-SNR slope and power offset of the SR achieved by the S-C design are given by L^{-1} and $\log_2 \left(\frac{16\pi^2 \sigma_s^2 r_s^4}{L\alpha_s \alpha_0^2 N^2} \right)$, respectively.

We next analyze the communication performance under the S-C design. By inserting $\mathbf{w} = \mathbf{h}_s \|\mathbf{h}_s\|^{-1}$ into (16), we obtain the CR as follows:

$$\bar{\mathcal{R}}_{d,c}^s = \log_2(1 + p/\sigma_c^2 \|\mathbf{h}_s\|^{-2} |\mathbf{h}_s^H \mathbf{h}_c|^2). \quad (23)$$

The following theorem provides a closed-form expression for the ECR $\mathcal{R}_{d,c}^s = \mathbb{E}\{\bar{\mathcal{R}}_{d,c}^s\}$ and its high-SNR approximation.

Theorem 2. The ECR achieved by the S-C design is

$$\mathcal{R}_{d,c}^s = -\frac{1}{\ln 2} e^{\sigma_c^2 \Omega / p} \text{Ei}(-\sigma_c^2 \Omega / p), \quad (24)$$

where $\Omega = \frac{N}{\mathbf{b}^H \mathbf{R} \mathbf{b}}$ with $[\mathbf{b}]_n = e^{-jk_0 \|\mathbf{r}_s - \mathbf{p}_n\|}$ for $n = 1, \dots, N$, and $\text{Ei}(x) = -\int_{-x}^{\infty} \frac{e^{-t}}{t} dt$ is the exponential integral function. When $p \rightarrow \infty$, the ECR satisfies

$$\mathcal{R}_{d,c}^s \approx \log_2 p - \log_2 \sigma_c^2 - \log_2 \Omega - \mathcal{C} / \ln 2, \quad (25)$$

where \mathcal{C} is the Euler constant.

Proof: Please refer to Appendix B for more details. ■

Remark 2. The results in Theorem 2 suggest that the high-SNR slope and power offset of the ECR achieved by the S-C design are given by 1 and $\log_2(\sigma_c^2 \Omega) + \frac{\mathcal{C}}{\ln 2}$, respectively.

Furthermore, the OP of the CR is defined as follows:

$$\mathcal{P}_d^s = \Pr(\bar{\mathcal{R}}_{d,c}^s < \mathcal{R}_0), \quad (26)$$

where $\mathcal{R}_0 > 0$ is the target rate. The following theorem provides a closed-form expression for the OP as well as its high-SNR approximation.

Theorem 3. The OP achieved by the S-C design is given by

$$\mathcal{P}_d^s = 1 - e^{-\sigma_c^2 \Omega (2^{\mathcal{R}_0} - 1) / p}. \quad (27)$$

When $p \rightarrow \infty$, the OP satisfies

$$\mathcal{P}_d^s \approx \sigma_c^2 \Omega (2^{\mathcal{R}_0} - 1) / p. \quad (28)$$

Proof: Please refer to Appendix B for more details. ■

Remark 3. The results in Theorem 3 suggest that the diversity order and array gain of the OP achieved by the S-C design are given by 1 and $\sigma_c^2 \Omega^{-1} (2^{\mathcal{R}_0} - 1)^{-1}$, respectively.

2) *Communications-Centric Design:* Next we focus on the C-C design. With I-CSI, the beamforming vector that maximizes the downlink CR is given by

$$\mathbf{w} = \arg\max_{\|\mathbf{w}\|^2=1} \bar{\mathcal{R}}_{d,c} \quad (29)$$

$$= \arg\max_{\|\mathbf{w}\|^2=1} |\mathbf{w}^H \mathbf{h}_c|^2 = \mathbf{h}_c \|\mathbf{h}_c\|^{-1}. \quad (30)$$

Upon substituting $\mathbf{w} = \mathbf{h}_c \|\mathbf{h}_c\|^{-1}$ into (16), we express the CR as follows:

$$\bar{\mathcal{R}}_{d,c}^c = \log_2(1 + p/\sigma_c^2 \|\mathbf{h}_c\|^2), \quad (31)$$

A closed-form expression for the OP $\mathcal{P}_d^c = \Pr(\bar{\mathcal{R}}_{d,c}^c < \mathcal{R}_0)$ is given as follows.

Theorem 4. The OP achieved by the C-C design is given by

$$\mathcal{P}_d^c = \frac{\lambda_n}{\prod_{n=1}^n \lambda_n} \sum_{k=0}^{\infty} \frac{\delta_k \Upsilon(n+k, \sigma_c^2 / p \lambda_n^{-1} (2^{\mathcal{R}_0} - 1))}{(n+k-1)!}, \quad (32)$$

where $\Upsilon(s, x) = \int_0^x t^{s-1} e^{-t} dt$ denotes the lower incomplete gamma function, $\delta_0 = 1$, and δ_k ($k > 0$) can be calculated

recursively as $\delta_k = \frac{1}{k} \sum_{i=1}^k [\sum_{n=1}^n (1 - \lambda_n / \lambda_n)^i] \delta_{k-i}$. When $p \rightarrow \infty$, the OP satisfies

$$\mathcal{P}_d^c \approx \frac{(2^{\mathcal{R}_0} - 1)^n \sigma_c^{2n}}{p^n n! \prod_{n=1}^n \lambda_n}. \quad (33)$$

Proof: Please refer to Appendix C for more details. ■

Remark 4. The results in Theorem 4 suggest that the diversity order and array gain of the OP achieved by the C-C design are given by n and $(n! \prod_{n=1}^n \lambda_n)^{\frac{1}{n}} \sigma_c^{-2} (2^{\mathcal{R}_0} - 1)^{-1}$, respectively.

We next turn our attention to the ECR $\mathcal{R}_{d,c}^c = \mathbb{E}\{\bar{\mathcal{R}}_{d,c}^c\}$. Let us define

$$\begin{aligned} \zeta(\mathbf{A}, a) &= \frac{\lambda_{A,r}^r \log_2 e}{\prod_{r=1}^r \lambda_{A,r}} \sum_{k=0}^{\infty} \sum_{\mu=0}^{r+k-1} \frac{\delta_k}{(r+k-1-\mu)!} \\ &\times \left[\frac{(-1)^{r+k-\mu} e^{1/a \lambda_{A,r}^{-1}} \text{Ei}\left(-\frac{1}{a \lambda_{A,r}}\right)}{(a \lambda_{A,r})^{r+k-1-\mu}} \right. \\ &\left. + \sum_{u=1}^{r+k-1-\mu} (u-1)! \left(-\frac{1}{a \lambda_{A,r}}\right)^{r+k-1-\mu-u} \right], \end{aligned} \quad (34)$$

where $\lambda_{A,1} \geq \dots \geq \lambda_{A,r}$ denote the positive eigenvalues of the matrix \mathbf{A} with $r = \text{rank}(\mathbf{A})$.

Theorem 5. The ECR achieved by the C-C design is

$$\mathcal{R}_{d,c}^c = \zeta(\mathbf{R}, p/\sigma_c^2). \quad (35)$$

When $p \rightarrow \infty$, the ECR satisfies

$$\mathcal{R}_{d,c}^c \approx \log_2 p - \log_2 \sigma_c^2 + v_{\mathbf{R}}. \quad (36)$$

where $v_{\mathbf{R}} = \frac{\lambda_n \log_2 e}{\prod_{n=1}^n \lambda_n} \sum_{k=0}^{\infty} \delta_k (\psi(n+k) + \ln(\lambda_n))$.

Proof: Please refer to Appendix C for more details. ■

Remark 5. The results in Theorem 5 suggest that the high-SNR slope and power offset of the ECR achieved by the C-C design are given by 1 and $\log_2 \sigma_c^2 - v_{\mathbf{R}}$, respectively.

By substituting $\mathbf{w} = \mathbf{h}_c \|\mathbf{h}_c\|^{-1}$ into (8), we obtain the SR as follows:

$$\bar{\mathcal{R}}_{d,s}^c = \frac{1}{L} \log_2 \left(1 + \frac{p}{\sigma_s^2} L \alpha_s \|\mathbf{h}_s\|^2 \frac{|\mathbf{h}_c^H \mathbf{h}_s|^2}{\|\mathbf{h}_c\|^2} \right). \quad (37)$$

To account for the statistics of \mathbf{h}_c , we define the average SR as $\mathcal{R}_{d,s}^c \triangleq \mathbb{E}\{\bar{\mathcal{R}}_{d,s}^c\}$ to assess the sensing performance.

Theorem 6. The average SR achieved by the C-C design is

$$\mathcal{R}_{d,s}^c = L^{-1} (v_{\Delta} - v_{\mathbf{R}}), \quad (38)$$

where v_{Δ} is obtained by replacing $\{\lambda_n\}_{n=1}^n$ in $v_{\mathbf{R}}$ with the positive eigenvalues of $\Delta = \mathbf{R}^{\frac{1}{2}} (p/\sigma_s^2 L \alpha_s \|\mathbf{h}_s\|^2 \mathbf{h}_s \mathbf{h}_s^H + \mathbf{I}) \mathbf{R}^{\frac{1}{2}}$. When $p \rightarrow \infty$, the average SR satisfies

$$\mathcal{R}_{d,s}^c \approx L^{-1} (\log_2 p - \log_2 \Xi - \mathcal{C} / \ln 2 - v_{\mathbf{R}}), \quad (39)$$

where $\Xi = \frac{16\pi^2 \sigma_s^2 r_s^4}{L \alpha_s \alpha_0^2 N^2} \Omega$.

Proof: Please refer to Appendix D for more details. ■

Remark 6. The results in Theorem 6 suggest that the high-SNR slope and power offset of the SR achieved by the S-C design are given by $\frac{1}{L}$ and $\log_2 \Xi + \frac{\mathcal{C}}{\ln 2} + v_{\mathbf{R}}$, respectively.

Remark 7. The above arguments imply that for downlink ISAC with I-CSI, the beamforming design *does not affect the high-SNR slope*, but it *does impact the diversity order, array gain, and high-SNR power offset*. Since $n \geq 1$, the C-C design can achieve a higher diversity order than the S-C design.

3) *Pareto Optimal Design:* In practical scenarios, the beamforming vector \mathbf{w} can be customized to meet diverse quality-

of-service requirements, introducing a trade-off between S&C performance. To evaluate this trade-off, we investigate the Pareto boundary of the SR-CR region. Specifically, the Pareto boundary comprises SR-CR pairs where it is impossible to enhance one of the rates without simultaneously reducing the other [24]. Any rate pair situated on this boundary can be identified by solving the following problem: [24]

$$\max_{\mathbf{w}, \mathcal{R}} \mathcal{R} \quad (40a)$$

$$\text{s.t. } L^{-1} \log_2(1 + p/\sigma_s^2 L \alpha_s \|\mathbf{h}_s\|^2 |\mathbf{w}^H \mathbf{h}_s|^2) \geq \tau \mathcal{R}, \quad (40b)$$

$$\log_2(1 + p/\sigma_c^2 |\mathbf{w}^H \mathbf{h}_c|^2) \geq (1 - \tau) \mathcal{R}, \quad (40c)$$

$$\|\mathbf{w}\|^2 = 1, \quad (40d)$$

where $\tau \in [0, 1]$ denotes a particular rate-profile parameter. The complete Pareto boundary is obtained by solving the problem (40) with τ ranging from 0 to 1. The solution to problem (40) is given as follows.

Theorem 7. For a given τ , the optimal beamforming vector is given as (41), shown in at the bottom of this page, where $\eta = \|\mu_1 \sqrt{2^{(1-\tau)\mathcal{R}^*} - 1} \mathbf{h}_1 + \mu_2 \sqrt{2^{\tau L \mathcal{R}^*} - 1} \mathbf{h}_2 e^{-j\angle \rho}\|$, $\mathbf{h}_1 = \sqrt{p/\sigma_c^2} \mathbf{h}_c$, $\mathbf{h}_2 = \sqrt{\frac{p\alpha_0 L \alpha_s N}{4\pi\sigma_s^2 \tau^2}} \mathbf{h}_s$, $\rho = \mathbf{h}_1^H \mathbf{h}_2$, $\xi_1 = \|\mathbf{h}_1\|^2 - \sqrt{\frac{2^{(1-\tau)\mathcal{R}^*} - 1}{2^{\tau L \mathcal{R}^*} - 1}} |\rho|$, $\xi_2 = \|\mathbf{h}_2\|^2 - \sqrt{\frac{2^{\tau L \mathcal{R}^*} - 1}{2^{(1-\tau)\mathcal{R}^*} - 1}} |\rho|$, $\chi = \xi_1 2^{\tau L \mathcal{R}^*} \tau L \ln 2 + \xi_2 2^{(1-\tau)\mathcal{R}^*} (1 - \tau) \ln 2$, $\mu_1 = \frac{\xi_2}{\chi}$, $\mu_2 = \frac{\xi_1}{\chi}$, and \mathcal{R}^* is the solution to the equation in (E.11).

Proof: Please refer to Appendix E for more details. ■

Based on the above results, we can further deduce the following corollary.

Corollary 1. The whole Pareto boundary of the rate region can be achieved by the beamforming vector as follows:

$$\mathbf{w}_\varsigma = \frac{\varsigma \mathbf{h}_c + (1 - \varsigma) \mathbf{h}_s e^{-j\angle \rho}}{\|\varsigma \mathbf{h}_c + (1 - \varsigma) \mathbf{h}_s e^{-j\angle \rho}\|}, \quad (42)$$

where $\varsigma \in [0, 1]$ is the weighting factor.

Proof: Please refer to Appendix F for more details. ■

Remark 8. The results in **Corollary 1** suggest that \mathbf{w}_ς can represent the normalization of any arbitrary linear combination of \mathbf{h}_c and $\mathbf{h}_s e^{-j\angle \rho}$ with non-negative real coefficients. This means that the Pareto optimal beamforming vector lies in the plane spanned by \mathbf{h}_c and $\mathbf{h}_s e^{-j\angle \rho}$.

Given τ , let $\mathcal{R}_{d,s}^\tau$ and $\mathcal{R}_{d,c}^\tau$ denote the SR and the CR achieved by Pareto optimal beamforming vector \mathbf{w}_τ , respectively. Accordingly, we have $\mathcal{R}_{d,s}^\tau \in [\overline{\mathcal{R}}_{d,s}^c, \mathcal{R}_{d,s}^s]$ and $\mathcal{R}_{d,c}^\tau \in [\overline{\mathcal{R}}_{d,c}^s, \overline{\mathcal{R}}_{d,c}^c]$ with $\mathcal{R}_{d,s}^0 = \overline{\mathcal{R}}_{d,s}^c$, $\mathcal{R}_{d,s}^1 = \mathcal{R}_{d,s}^s$, $\mathcal{R}_{d,c}^0 = \overline{\mathcal{R}}_{d,c}^c$, and $\mathcal{R}_{d,c}^1 = \overline{\mathcal{R}}_{d,c}^s$. By exploiting the Sandwich theorem, the high-SNR slopes and diversity orders of any SR-CR pair on the Pareto boundary can be obtained. Finally, letting $(\mathcal{R}_s, \mathcal{R}_c)$ denote the achievable SR-CR pair, the SR-CR region achieved

by near-field HISAC with I-CSI can be written as follows:

$$\mathcal{C}_d = \left\{ (\mathcal{R}_s, \mathcal{R}_c) \left| \begin{array}{l} \mathcal{R}_s \in [0, \mathcal{R}_{d,s}^\tau], \mathcal{R}_c \in [0, \mathcal{R}_{d,c}^\tau], \\ \tau \in [0, 1] \end{array} \right. \right\}. \quad (43)$$

B. Statistical CSI

Having investigated the I-CSI case, we now move to the S-CSI case where the BS has no knowledge of \mathbf{h}_c and only knows \mathbf{R} .

1) *Sensing-Centric Design:* Since the optimal beamforming vector under the S-C design, i.e., $\mathbf{h}_s \|\mathbf{h}_s\|^{-1}$, is independent of \mathbf{h}_c , the S&C performance of the S-C design in the S-CSI case is the same as that in the I-CSI case.

2) *Communications-Centric Design:* Since the instantaneous information of \mathbf{h}_c is unknown to the BS, the C-C beamforming vector is set to maximize the ECR instead of the instantaneous CR. As a result, the optimal beamforming vector satisfies

$$\mathbf{w} = \operatorname{argmax}_{\|\mathbf{w}\|^2=1} \mathbb{E}\{\overline{\mathcal{R}}_{d,c}\} \quad (44)$$

$$= \operatorname{argmax}_{\|\mathbf{w}\|^2=1} \mathbb{E}\{\log_2(1 + p/\sigma_c^2 |\mathbf{w}^H \mathbf{h}_c|^2)\}. \quad (45)$$

The solution to the above problem is summarized as follows.

Lemma 2. The optimal beamforming vector under the C-C design with S-CSI is given by the normalized principal eigenvector of \mathbf{R} , i.e., $\mathbf{a}(m_x^*, m_y^*) \triangleq \mathbf{a}_*$, where

$$(m_x^*, m_y^*) = \operatorname{argmax}_{(m_x, m_y) \in \mathcal{E}} \sigma^2(m_x, m_y). \quad (46)$$

Proof: Please refer to Appendix G for more details. ■

By setting $\mathbf{w} = \mathbf{a}_*$, we obtain

$$\mathbf{a}_*^H \mathbf{R} \mathbf{a}_* = \max_{(m_x, m_y) \in \mathcal{E}} \sigma^2(m_x, m_y) = \lambda_1. \quad (47)$$

We then present the analytical results for the ECR and OP in the following theorems.

Theorem 8. With S-CSI, the ECR achieved by the C-C design can be written as follows:

$$\mathcal{R}_{d,c}^c = -e^{\sigma_c^2 \lambda_1^{-1}/p} \operatorname{Ei}(-\sigma_c^2 \lambda_1^{-1}/p) \log_2 e. \quad (48)$$

When $p \rightarrow \infty$, the ECR satisfies

$$\mathcal{R}_{d,c}^c \approx \log_2 p - \log_2 \sigma_c^2 + \log_2 \lambda_1 - \mathcal{C}/\ln 2. \quad (49)$$

Proof: Similar to the proof of **Theorem 2**. ■

Theorem 9. With S-CSI, the OP achieved by the C-C design can be written as follows:

$$\mathcal{P}_d^c = 1 - e^{-\sigma_c^2 \lambda_1^{-1} (2^{\mathcal{R}_0} - 1)/p}. \quad (50)$$

When $p \rightarrow \infty$, the OP satisfies

$$\mathcal{P}_d^c \approx \sigma_c^2 \lambda_1^{-1} (2^{\mathcal{R}_0} - 1)/p. \quad (51)$$

Proof: Similar to the proof of **Theorem 3**. ■

Remark 9. The results in **Theorem 8** and **9** suggest that the high-SNR slope and diversity order of the CR achieved by the C-C design with S-CSI are both equal to 1.

$$\mathbf{w}_\tau = \begin{cases} \mathbf{h}_c \|\mathbf{h}_c\|^{-1}, & \tau \in \left[0, \frac{\overline{\mathcal{R}}_{d,s}^c}{\overline{\mathcal{R}}_{d,c}^c + \overline{\mathcal{R}}_{d,s}^c}\right] \\ \frac{\mu_1 \sqrt{2^{(1-\tau)\mathcal{R}^*} - 1}}{\eta} \mathbf{h}_1 + \frac{\mu_2 \sqrt{2^{\tau L \mathcal{R}^*} - 1}}{\eta} \mathbf{h}_2 e^{-j\angle \rho}, & \tau \in \left(\frac{\overline{\mathcal{R}}_{d,s}^c}{\overline{\mathcal{R}}_{d,c}^c + \overline{\mathcal{R}}_{d,s}^c}, \frac{\mathcal{R}_{d,s}^s}{\overline{\mathcal{R}}_{d,c}^c + \mathcal{R}_{d,s}^s}\right) \\ \mathbf{h}_s \|\mathbf{h}_s\|^{-1}, & \tau \in \left[\frac{\mathcal{R}_{d,s}^s}{\overline{\mathcal{R}}_{d,c}^c + \mathcal{R}_{d,s}^s}, 1\right] \end{cases}. \quad (41)$$

In the sequel, we analyze the SR achieved by the C-C design under the S-CSI case.

Theorem 10. Let us define $\Gamma \triangleq \frac{L\alpha_s\alpha_n^2N}{16\pi^2r^4} \left| \sum_{n=1}^N a_b^* \left(\frac{2\pi m_x}{L_x}, \frac{2\pi m_y}{L_y}, \mathbf{p}_n \right) e^{-jk_0 r_{c,z} - jk_0 \|\mathbf{r}_s - \mathbf{p}_n\|} \right|^2$. The SR achieved by the C-C design with S-CSI can be written as follows:

$$\mathcal{R}_{d,s}^c = L^{-1} \log_2 (1 + p/\sigma_s^2 \Gamma), \quad (52)$$

When $p \rightarrow \infty$, the SR satisfies

$$\mathcal{R}_{d,s}^c \approx L^{-1} \log_2 p + L^{-1} \log_2 (\Gamma/\sigma_s^2). \quad (53)$$

Proof: Similar to the proof of **Theorem 1**. ■

Remark 10. The results in **Theorem 10** suggest that the high-SNR slope and power offset of the SR achieved by the C-C design with S-CSI are given by $1/L$ and $\log_2(\sigma_s^2/\Gamma)$, respectively.

In addition to this, the following conclusion can be found.

Remark 11. The above arguments imply that for downlink ISAC with S-CSI, the beamforming design *does not affect the high-SNR slope and diversity order*, but it does *impact the array gain and high-SNR power offset*. Specifically, under the C-C design, the diversity order achieved with I-CSI is higher than that achieved with S-CSI.

3) *Pareto Optimal Design:* We next characterize the downlink rate region in the case of S-CSI. Based on the proof in Appendix G, the ECR $\mathbb{E}\{\bar{\mathcal{R}}_{d,c}\}$ is monotonically increasing with $\mathbf{w}^H \mathbf{R} \mathbf{w}$. As a result, the rate region can be characterized by first solving the following problem:

$$\max_{\mathbf{w}, x} \quad (54a)$$

$$\text{s.t.} \quad \mathbf{w}^H \mathbf{R} \mathbf{w} \geq (1 - \tau)x, |\mathbf{w}^H \mathbf{h}_s|^2 \geq \tau x, \|\mathbf{w}\|^2 = 1 \quad (54b)$$

for $\tau \in [0, 1]$, and then calculating the corresponding SR-ECR pair. By defining $\mathbf{W} \triangleq \mathbf{w} \mathbf{w}^H$ and $\mathbf{H} \triangleq \mathbf{h}_s \mathbf{h}_s^H$, problem (54) can be rewritten as follows:

$$\max_{\mathbf{W}, x} \quad (55a)$$

$$\text{s.t.} \quad \text{tr}(\mathbf{R} \mathbf{W}) \geq (1 - \tau)x, \text{tr}(\mathbf{H} \mathbf{W}) \geq \tau x, \quad (55b)$$

$$\text{tr}(\mathbf{W}) = 1, \mathbf{W} \succeq \mathbf{0}, \text{rank}(\mathbf{W}) = 1, \quad (55c)$$

which is a non-convex problem whose optimal solution generally requires a brute-force search. Let $(\mathcal{R}_{d,s}^\tau, \mathcal{R}_{d,c}^\tau)$ denote the optimal SR-CR pair corresponding to τ . Then the high-SNR slopes and diversity orders of $(\mathcal{R}_{d,s}^\tau, \mathcal{R}_{d,c}^\tau)$ can be derived by using the Sandwich theorem. Besides, the rate region can be characterized as follows:

$$\mathcal{C}_d = \left\{ (\mathcal{R}_s, \mathcal{R}_c) \left| \begin{array}{l} \mathcal{R}_s \in [0, \mathcal{R}_{d,s}^\tau], \mathcal{R}_c \in [0, \mathcal{R}_{d,c}^\tau], \\ \tau \in [0, 1] \end{array} \right. \right\}. \quad (56)$$

Unfortunately, obtaining the entire rate region is computationally inefficient. As a compromise, we next provide an inner bound of the rate region. The non-convexity of (55) lies in the rank-one constraint $\text{rank}(\mathbf{W}) = 1$. For this constraint, the conventional approach is applying semidefinite relaxation (SDR), where we first solve the problem by ignoring the rank-one constraint, and then construct a rank-one solution with Gaussian randomization method if the solution obtained from the relaxed problem is not rank-one [25]. Let $\bar{\mathcal{C}}_d$ denote the SR-CR region achieved by the SDR-based method. Then we have $\bar{\mathcal{C}}_d \subseteq \mathcal{C}_d$. The boundary of $\bar{\mathcal{C}}_d$ thus serves an inner

Design	Sensing		Communications			
	I-CSI	S-CSI	I-CSI		S-CSI	
	\mathcal{S}	\mathcal{S}	\mathcal{S}	\mathcal{D}	\mathcal{S}	\mathcal{D}
S-C	$1/L$	$1/L$	1	1	1	1
C-C	$1/L$	$1/L$	1	n	1	1
Pareto Optimal	$1/L$	$1/L$	1	[1, n]	1	1
FDSAC	$(1-\kappa)/L$	$(1-\kappa)/L$	κ	n	κ	1

TABLE I: Downlink High-SNR Slope (\mathcal{S}) and Diversity Order (\mathcal{D}) with I-CSI and S-CSI

bound for $\bar{\mathcal{C}}_d$, whose tightness will be verified by the numerical results presented in Section V.

C. Baseline: FDSAC

We consider FDSAC as a baseline scenario, where $\kappa \in [0, 1]$ fraction of the total bandwidth and $\iota \in [0, 1]$ fraction of the total power is used for communications, and the other is used for sensing. Consequently, the SR achieved by FDSAC is given by $\mathcal{R}_{d,s}^f = \frac{1-\kappa}{L} \log_2 (1 + \frac{1-\iota}{1-\kappa} p/\sigma_s^2 L \alpha_s \|\mathbf{h}_s\|^4)$. As for communications, the CRs in the cases of I-CSI and S-CSI can be written as $\mathcal{R}_{d,c}^f = \kappa \log_2 (1 + \frac{\iota}{\kappa} p/\sigma_c^2 \|\mathbf{h}_c\|^2)$ and $\mathcal{R}_{d,c}^f = \kappa \log_2 (1 + \frac{\iota}{\kappa} p/\sigma_c^2 |\mathbf{a}_*^H \mathbf{h}_c|^2)$, respectively. Note that the CR and SR achieved by FDSAC can be analyzed in a similar way we analyze those achieved by ISAC. For the sake of reference, we summarize the results related to diversity order and high-SNR slope in Table I.

Remark 12. The results in Table I indicate that ISAC can achieve higher high-SNR slopes for both downlink SR and CR than FDSAC, providing more DoFs in terms of both S&C.

Moreover, the SR-CR region of downlink FDSAC satisfies

$$\mathcal{C}_d^f = \left\{ (\mathcal{R}_s, \mathcal{R}_c) \left| \begin{array}{l} \mathcal{R}_s \in [0, \mathcal{R}_{d,s}^f], \mathcal{R}_c \in [0, \mathcal{R}_{d,c}^f], \\ \kappa \in [0, 1], \iota \in [0, 1] \end{array} \right. \right\}. \quad (57)$$

IV. UPLINK PERFORMANCE ANALYSIS

Having analyzed the downlink performance of near-field HISAC, we now shift our focus on the uplink performance.

A. Instantaneous CSI

1) *Communications-Centric SIC:* Let us first study the sensing performance achieved by the C-C SIC, where the target response signal is firstly estimated by regarding the communication signal as interference. From a worst-case design perspective, we can treat the aggregate interference-plus-noise $\mathbf{Z}_c = \sqrt{p_c} \mathbf{h}_c \mathbf{s}_c^H + \mathbf{N}_u$ as the Gaussian noise [26]. Under this consideration, we conclude the following lemma.

Lemma 3. The SR achieved by the C-C SIC is given by
$$\bar{\mathcal{R}}_{u,s}^c = \frac{1}{L} \log_2 \left[1 + \frac{p_s L \alpha_s |\mathbf{h}_s^H \mathbf{w}|^2}{\sigma_u^2} \left(\|\mathbf{h}_s\|^2 - \frac{p_c |\mathbf{h}_s^H \mathbf{h}_c|^2}{p_c \|\mathbf{h}_c\|^2 + \sigma_u^2} \right) \right]. \quad (58)$$

Proof: Please refer to Appendix H for more details. ■

The results in **Lemma 3** suggest that the SR is maximized when $\mathbf{w} = \mathbf{h}_s \|\mathbf{h}_s\|^{-1}$. The following theorem provide a closed-form expression for the average SR $\bar{\mathcal{R}}_{u,s}^c = \mathbb{E}\{\bar{\mathcal{R}}_{u,s}^c\}$ and its high-SNR approximation.

Theorem 11. The average SR achieved by the C-C SIC is

$$\mathcal{R}_{u,s}^c = \frac{1}{L} \left[\zeta \left(\Theta, \frac{p_c}{\sigma_u^2} \Psi^{-1} \right) - \zeta \left(\mathbf{R}, \frac{p_c}{\sigma_u^2} \right) + \log_2 \Psi \right], \quad (59)$$

where $\Theta = \mathbf{R} + \frac{p_s}{\sigma_u^2} L \alpha_s \|\mathbf{h}_s\|^2 \mathbf{R}^{\frac{1}{2}} (\|\mathbf{h}_s\|^2 \mathbf{I}_N - \mathbf{h}_s \mathbf{h}_s^H) \mathbf{R}^{\frac{1}{2}} \succeq \mathbf{0}$, and $\Psi = \frac{p_s}{\sigma_u^2} L \alpha_s \|\mathbf{h}_s\|^4 + 1$. When $p_s \rightarrow \infty$, its high-SNR approximation satisfies

$$\mathcal{R}_{u,s}^c \approx \frac{1}{L} \left[\log_2 p_s + \zeta \left(\tilde{\Theta}, \frac{p_c}{\sigma_u^2 \tilde{\Psi}} \right) - \zeta \left(\mathbf{R}, \frac{p_c}{\sigma_u^2} \right) + \log_2 \tilde{\Psi} \right], \quad (60)$$

where $\tilde{\Theta} = L \alpha_s \|\mathbf{h}_s\|^2 \mathbf{R}^{\frac{1}{2}} (\|\mathbf{h}_s\|^2 \mathbf{I}_N - \mathbf{h}_s \mathbf{h}_s^H) \mathbf{R}^{\frac{1}{2}}$, and $\tilde{\Psi} = L \alpha_s \|\mathbf{h}_s\|^4 / \sigma_u^2$.

Proof: Similar to the proof of **Theorem 6**. ■

Remark 13. **Theorem 11** suggests that the high-SNR slope of the SR achieved by the C-C SIC is given by $1/L$.

After estimating the target response, the echo signal $\sqrt{p_s} \mathbf{G} \mathbf{w} \mathbf{s}_s^H$ can be removed from the received superposed S&C signal. The remaining communication signal is then decoded using the optimal detection vector $\frac{\mathbf{h}_c}{\|\mathbf{h}_c\|}$. Consequently, the CR is given by $\bar{\mathcal{R}}_{u,c}^c = \log_2(1 + \frac{p_c}{\sigma_u^2} \|\mathbf{h}_c\|^2)$. In this scenario, the ECR $\mathcal{R}_{u,c}^c = \mathbb{E}\{\bar{\mathcal{R}}_{u,c}^c\}$ and the OP $\mathcal{P}_u^c = \Pr(\bar{\mathcal{R}}_{u,c}^c < \mathcal{R}_0)$ can be analyzed in a similar way we analyze those achieved by the downlink C-C design with I-CSI. Further details are omitted for brevity.

B. Sensing-Centric SIC

In the context of S-C SIC, the BS first detects the communication signal from the CU, considering the echo signal $\sqrt{p_s} \mathbf{G} \mathbf{w} \mathbf{s}_s^H$ as interference. From a worst-case design perspective, the aggregate interference-plus-noise $\mathbf{Z}_s = \sqrt{p_s} \mathbf{G} \mathbf{w} \mathbf{s}_s^H + \mathbf{N}_u$ is treated as the Gaussian noise [26]. Under this circumstance, the uplink ECR and OP are given in the following theorems, respectively.

Theorem 12. The uplink ECR of the S-C design is given by

$$\mathcal{R}_{u,c}^s = \zeta(\Phi, p_c / \sigma_u^2), \quad (61)$$

where $\Phi = \mathbf{R}^{\frac{1}{2}} (p_s / \sigma_u^2 \alpha_s \|\mathbf{h}_s\|^2 \mathbf{h}_s \mathbf{h}_s^H + \mathbf{I})^{-1} \mathbf{R}^{\frac{1}{2}} \succeq \mathbf{0}$. When $p_c \rightarrow \infty$, the ECR satisfies

$$\mathcal{R}_{u,c}^s \approx \log_2 p_c - \log_2 \sigma_u^2 + v_\Phi, \quad (62)$$

where v_Φ is obtained by replacing $\{\lambda_n\}_{n=1}^n$ in $v_{\mathbf{R}}$ with the positive eigenvalues of Φ .

Proof: Please refer to Appendix I for more details. ■

Theorem 13. The OP achieved by the S-C SIC is written as

$$\mathcal{P}_u^s = \frac{\lambda_{\Phi,m}^m}{\prod_{m=1}^m \lambda_{\Phi,m}} \sum_{k=0}^{\infty} \frac{\delta'_k \Upsilon(m+k, \sigma_u^2 / p_c \lambda_{\Phi,m}^{-1} (2^{\mathcal{R}_0} - 1))}{(m+k-1)!}, \quad (63)$$

where $\lambda_{\Phi,1} \geq \dots \geq \lambda_{\Phi,m}$ denote the positive eigenvalues of the matrix Φ with $m = \text{rank}(\Phi) \leq N$, $\delta'_0 = 1$, and δ'_k ($k > 0$) can be obtained recursively by $\delta'_k = \frac{1}{k} \sum_{i=1}^k [\sum_{m=1}^m (1 - \lambda_{\Phi,m} / \lambda_{\Phi,m})^i] \delta'_{k-i}$. When $p_c \rightarrow \infty$, the OP satisfies

$$\mathcal{P}_u^s \approx \frac{(2^{\mathcal{R}_0} - 1)^m \sigma_u^{2m}}{p_c^m m! \prod_{m=1}^m \lambda_{\Phi,m}}. \quad (64)$$

Proof: Similar to the proof of **Theorem 4**. ■

Remark 14. The results in **Theorem 13** suggest that the diversity order and array gain of the OP achieved by the S-C

sic are given by m and $(m! \prod_{m=1}^m \lambda_{\Phi,m})^{\frac{1}{m}} \sigma_u^{-2} (2^{\mathcal{R}_0} - 1)^{-1}$, respectively.

After detecting the communication signal, the BS subtracts it from the received signal, utilizing the remaining part to extract information from the target response matrix \mathbf{G} , which yields a same SR as in **Theorem 1**, i.e., $\mathcal{R}_{u,s}^c = \mathcal{R}_{d,s}^s$.

Remark 15. For the uplink scenario with I-CSI, the SIC order does not affect the high-SNR slopes of both the CR and SR, whereas it does affect the diversity order and high-SNR slope. Specifically, since $m = \text{rank}(\Phi) \leq \text{rank}(\mathbf{R}) = n$, the diversity order achieved by the C-C SIC is no smaller than that achieved by the S-C SIC.

C. Statistic CSI

Having investigated the S&C performance in the case of I-CSI, we shift our focus to the case of S-CSI. In this scenario, the BS lacks complete knowledge of the communication channel \mathbf{h}_c . Consequently, the BS can only utilize the S-CSI to design the detection vector for the communication signal, which is denoted as \mathbf{v} . It is assumed that the BS possesses knowledge of the effective channel $\mathbf{v}^H \mathbf{h}_c \in \mathbb{C}$, the acquisition of which incurs significantly lower signaling overhead than obtaining \mathbf{h}_c .

1) *Communications-Centric SIC:* We commence by analyzing the SR achieved by the C-C SIC.

Theorem 14. By treating \mathbf{Z}_c as Gaussian noise, the SR is given by

$$\mathcal{R}_{u,s}^c = L^{-1} \log_2 \left(1 + p_s L \alpha_s \|\mathbf{h}_s\|^2 \mathbf{h}_s^H (p_c \mathbf{R} + \sigma_u^2 \mathbf{I})^{-1} \mathbf{h}_s \right). \quad (65)$$

When $p_s \rightarrow \infty$, the SR satisfies

$$\mathcal{R}_{u,s}^c \approx L^{-1} \log_2 p_s + L^{-1} \log_2 (L \alpha_s \|\mathbf{h}_s\|^2 \mathbf{h}_s^H (p_c \mathbf{R} + \sigma_u^2 \mathbf{I})^{-1} \mathbf{h}_s). \quad (66)$$

Proof: Similar to the proof of **Theorem 11**. ■

Remark 16. **Theorem 14** suggests that the high-SNR slope of the SR achieved by the C-C SIC is given by L^{-1} .

After estimating the target response, the echo signal can be removed from \mathbf{Y}_u with the remaining communication signal being without interference. The resulting ECR $\mathcal{R}_{u,c}^c$ and OP can thus be analyzed by following similar steps shown in **Theorem 8** and **9**, respectively.

2) *Sensing-Centric SIC:* Then we move to the S-C design where the communication signal is first detected by considering the echo signal as interference. Under the S-C design, the uplink CR is written as follows:

$$\bar{\mathcal{R}}_{u,c}^s = \log_2 \left(1 + \frac{p_c |\mathbf{v}^H \mathbf{h}_c|^2}{p_s \alpha_s \|\mathbf{h}_s\|^2 |\mathbf{v}^H \mathbf{h}_s|^2 + \sigma_u^2} \right), \quad (67)$$

where \mathbf{v} denotes the communication detection vector with $\|\mathbf{v}\|^2 = 1$. Recalling that the BS only has the statistical information of \mathbf{h}_c , \mathbf{v} should be designed to maximize the ECR $\mathcal{R}_{u,c}^s = \mathbb{E}\{\bar{\mathcal{R}}_{u,c}^s\}$. The following lemma gives the optimal detection vector that maximizes the ECR.

Lemma 4. The optimal detection vector under the S-C design with S-CSI is given by

$$\mathbf{v}_\star = \frac{(p_s / \sigma_u^2 \alpha_s \|\mathbf{h}_s\|^2 \mathbf{h}_s \mathbf{h}_s^H + \mathbf{I})^{-\frac{1}{2}} \mathbf{u}_\star}{\mathbf{u}_\star^H (p_s / \sigma_u^2 \alpha_s \|\mathbf{h}_s\|^2 \mathbf{h}_s \mathbf{h}_s^H + \mathbf{I})^{-1} \mathbf{u}_\star}, \quad (68)$$

Design	Sensing		Communications			
	I-CSI	S-CSI	I-CSI	S-CSI		
	\mathcal{S}	\mathcal{S}	\mathcal{S}	\mathcal{D}	\mathcal{S}	\mathcal{D}
S-C	$1/L$	$1/L$	1	m	1	1
C-C	$1/L$	$1/L$	1	n	1	1
Time-Sharing	$1/L$	$1/L$	1	[m, n]	1	1
FDSAC	$(1-\kappa)/L$	$(1-\kappa)/L$	κ	n	κ	1

TABLE II: Uplink High-SNR Slope (\mathcal{S}) and Diversity Order (\mathcal{D}) with I-CSI and S-CSI

where \mathbf{u}_\star is the principal eigenvector of $(p_s/\sigma_u^2\alpha_s\|\mathbf{h}_s\|^2\mathbf{h}_s\mathbf{h}_s^H + \mathbf{I})^{-\frac{1}{2}}\mathbf{R}(p_s/\sigma_u^2\alpha_s\|\mathbf{h}_s\|^2\mathbf{h}_s\mathbf{h}_s^H + \mathbf{I})^{-\frac{1}{2}}$.

Proof: Please refer to Appendix J for more details. ■

By setting $\mathbf{v} = \mathbf{v}_\star$, the communication performance is studied in the following theorems.

Theorem 15. The uplink ECR achieved by the S-C design is derived as

$$\mathcal{R}_{u,c}^s = -\frac{1}{\ln 2} e^{\frac{\sigma_u^2}{p_c \kappa}} \text{Ei}\left(-\frac{\sigma_u^2}{p_c \kappa}\right). \quad (69)$$

When $p_c \rightarrow \infty$, the ECR satisfies

$$\mathcal{R}_{u,c}^s \approx \log_2 p_c - \log_2 \sigma_u^2 + \log_2 \kappa - \mathcal{C} \log_2 e. \quad (70)$$

Proof: Similar to the proof of **Theorem 2**. ■

Theorem 16. The OP of the S-C design is given by

$$\mathcal{P}_u^s = 1 - e^{-\frac{\sigma_u^2(2^{\mathcal{R}_0}-1)}{p_c \kappa}}. \quad (71)$$

When $p_c \rightarrow \infty$, the OP satisfies

$$\tilde{\mathcal{P}}_u^s \approx \frac{\sigma_u^2(2^{\mathcal{R}_0}-1)}{p_c \kappa}. \quad (72)$$

Proof: Similar to the proof of **Theorem 3**. ■

Remark 17. The results in **Theorem 15** and **16** suggest that the high-SNR slope and diversity order of the CR achieved by the S-C SIC with S-CSI are both equal to 1.

After decoding the communication signal, the sensing information can be estimated without interference, which yields a same average SR as in **Theorem 1**, i.e., $\mathcal{R}_{u,s}^s = \mathcal{R}_{d,s}^s$.

Based on the analysis above for the uplink near-field ISAC, we can make the following conclusion.

Remark 18. For the uplink scenario with S-CSI, the SIC order does not affect either the high-SNR slopes or diversity orders. Besides, I-CSI yields higher diversity orders than S-CSI.

D. Rate Region Characterization

To characterize the uplink SR-CR region, we utilize the time-sharing strategy [27], where the S-C SIC is applied with probability ϵ and the C-C SIC is applied with probability $1-\epsilon$. For a given ϵ , letting $(\mathcal{R}_{u,s}^\epsilon, \mathcal{R}_{u,c}^\epsilon)$ represent the achievable SR-CR pair, we have $\mathcal{R}_{u,s}^\epsilon = \epsilon \mathcal{R}_{u,s}^s + (1-\epsilon)\mathcal{R}_{u,s}^c$ and $\mathcal{R}_{u,c}^\epsilon = \epsilon \mathcal{R}_{u,c}^s + (1-\epsilon)\mathcal{R}_{u,c}^c$. By exploiting the sandwich theorem, we can obtain the high-SNR slopes and diversity orders of any uplink SR-CR pair achieved through the time-sharing strategy, which are summarized in Table II. Denoting the achievable SR-CR pair as $(\mathcal{R}_s, \mathcal{R}_c)$, the uplink rate regions achieved by near-field HISAC reads

$$\mathcal{C}_u = \left\{ (\mathcal{R}_s, \mathcal{R}_c) \left| \begin{array}{l} \mathcal{R}_{u,s} \in [0, \mathcal{R}_{u,s}^\epsilon], \mathcal{R}_{u,c} \in [0, \mathcal{R}_{u,c}^\epsilon], \\ \epsilon \in [0, 1] \end{array} \right. \right\}. \quad (73)$$

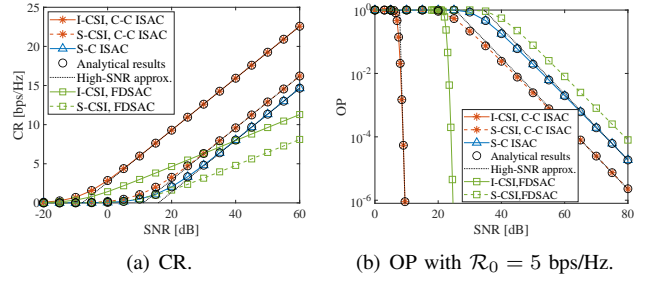


Fig. 2: Downlink communication performance.

E. Baseline: FDSAC

We consider FDSAC as the baseline scheme, wherein $\kappa \in [0, 1]$ fraction of the total bandwidth is allocated to communications, and the other is used for sensing. Consequently, the SR achieved by FDSAC is given by $\mathcal{R}_{u,s}^f = \frac{1-\kappa}{L} \log_2(1 + \frac{1}{1-\kappa} p_s/\sigma_u^2 L \alpha_s \|\mathbf{h}_s\|^4)$. As for communications, the CRs in the cases of I-CSI and S-CSI can be written as $\mathcal{R}_{u,c}^f = \kappa \log_2(1 + \frac{1}{\kappa} p_c/\sigma_u^2 \|\mathbf{h}_c\|^2)$ and $\mathcal{R}_{u,c}^f = \kappa \log_2(1 + \frac{1}{\kappa} p_c/\sigma_u^2 |\mathbf{v}_\star^H \mathbf{h}_c|^2)$, respectively. Note that the CR and SR achieved by FDSAC can be analyzed in a similar way we analyze those achieved by ISAC. For the sake of reference, we summarize the results related to diversity order and high-SNR slope in Table II.

Remark 19. The results in Table II indicate that ISAC can achieve higher high-SNR slopes for both uplink SR and CR than FDSAC, providing more DoFs in terms of both S&C.

Finally, the SR-CR region of uplink FDSAC satisfies

$$\mathcal{C}_u^f = \left\{ (\mathcal{R}_s, \mathcal{R}_c) \left| \begin{array}{l} \mathcal{R}_s \in [0, \mathcal{R}_{u,s}^f], \mathcal{R}_c \in [0, \mathcal{R}_{u,c}^f], \\ \kappa \in [0, 1] \end{array} \right. \right\}. \quad (74)$$

V. NUMERICAL RESULTS

In this section, numerical results are provided to evaluate the S&C performance of the proposed systems and verify the derived analytical results. Without otherwise specification, the simulation parameter settings are defined as follows: $\frac{\alpha_0}{\sigma_s^2} = \frac{\alpha_0}{\sigma_u^2} = 1$, $N_x = N_y = 20$, $\lambda = 0.125$ m, $d = \frac{\lambda}{4}$, $L = 4$, and $\kappa = \iota = 0.5$. The CU and the target are located at $\mathbf{r}_c = [1 \text{ m}, 1 \text{ m}, 5 \text{ m}]$ and $\mathbf{r}_s = [0 \text{ m}, 0 \text{ m}, 3 \text{ m}]$, respectively.

A. Downlink Performance

Fig. 2(a) and Fig. 2(b) plot the downlink CR and OP versus the communication SNR p/σ_c^2 , respectively. It can be seen that the C-C ISAC with I-CSI attains the highest communication performance, whereas FDSAC achieves the poorest OP and also the lowest CR for large values of p/σ_c^2 . The derived analytical results match the simulation results well, and the high-SNR approximations precisely follow the simulation results in the high-SNR regime. Moreover, it is worth noting that regardless of the CSI assumption, the CRs of both C-C ISAC and S-C ISAC exhibit the same high-SNR slope, which is higher than that of FDSAC. However, under the I-CSI case, the downlink diversity order achieved by the C-C ISAC is significantly higher than the S-C ISAC, while the diversity orders achieved by different designs with S-CSI are

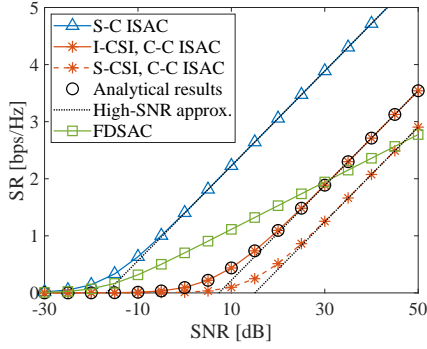
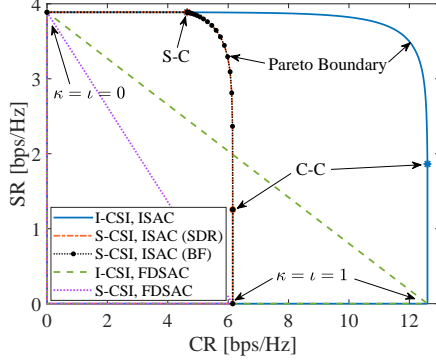


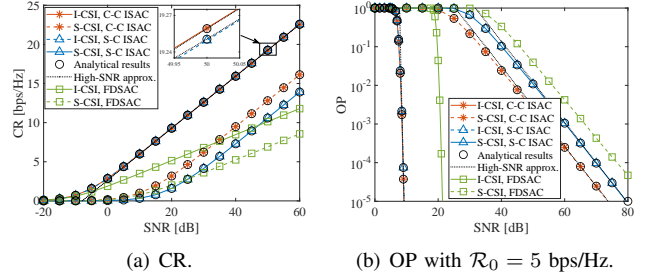
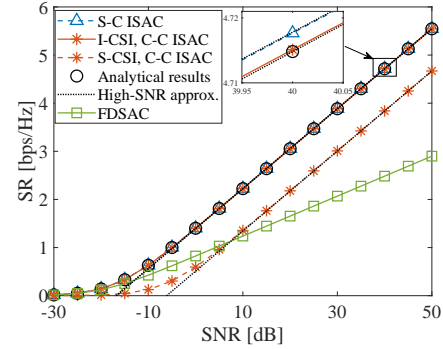
Fig. 3: Downlink SR.

Fig. 4: Downlink rate regions with $p/\sigma_s^2 = p/\sigma_c^2 = 30$ dB.

identical. These observations validate the conclusions drawn in **Remark 7** and **11**.

Fig. 3 shows the downlink SR versus the sensing SNR p/σ_s^2 , validating the accuracy of the analytical and approximated results. It is evident that S-C ISAC exhibits the most superior SR performance, while the SRs achieved by the S-C ISAC and the C-C ISAC yield the same high-SNR slope in both CSI cases. Through a joint examination of Fig. 2(a) and Fig. 3, we observe that both the CRs and SRs of ISAC demonstrate higher high-SNR slopes than FDSAC, aligning with the statement in **Remark 12**. Moreover, the CSI has no impact on ISAC performance under the S-C design, while it does influence the ISAC performance under the C-C design. Specifically, both CR and SR of the C-C design in the I-CSI case are larger than those in the S-CSI case, with the compensation of higher signaling overhead.

In Fig. 4, the downlink SR-CR regions achieved by the ISAC system and the baseline FDSAC system with different CSI are presented. For ISAC with either I-CSI or S-CSI, the two marked points on the graph represent the S-C and C-C designs, respectively. The curve section connecting the two points illustrates the Pareto boundary of the downlink ISAC's rate region, determined by solving either the problem (40) or (54) for values of τ ranging from 0 to 1. As anticipated, it is evident that with I-CSI, ISAC can achieve a more extensive rate region than in the S-CSI case. Additionally, it is crucial to emphasize that in both CSI scenarios, the downlink SR-CR region achieved by FDSAC is entirely encompassed by the rate region of ISAC. This observation underscores the superior S&C performance of ISAC compared to FDSAC. Last but not least, it can be seen from the above graph that for

Fig. 5: Uplink ECR and OP with $p_s/\sigma_u^2 = 30$ dB.Fig. 6: Uplink SR with $p_c/\sigma_u^2 = 30$ dB.

the S-CSI case, the rate region achieved by the SDR-based method is nearly coincident with that achieved by the brute-force (BF) search-based Pareto optimal design. This means that the rank-one relaxation in problem (55) is tight in our considered system.

B. Uplink Performance

Moving to the uplink results, we refer to Fig 5(a) and Fig 5(b), illustrating the uplink CR and OP with respect to the SNR p_c/σ_u^2 , respectively. The analytical results closely match the simulation results, and the high-SNR approximations accurately capture the behavior in the high-SNR region. Notably, despite C-C ISAC with I-CSI exhibits the highest CR, the performance gap between uplink C-C ISAC and S-C ISAC under the I-CSI case is remarkably small. This is attributed to the near-field effect, where the channel correlation between communication and sensing channels is close to zero within the near field [28]. This implies that the near-field effect can be effectively harnessed to mitigate the IFI, thereby enhancing uplink ISAC performance. Besides, we observe that the CR of ISAC yields an identical high-SNR slope with both I-CSI and S-CSI, which surpasses that achieved by FDSAC. On the other hand, the diversity orders achieved by ISAC with I-CSI are higher than those achieved under the S-CSI case, validating the discussions presented in **Remark 15** and **18**. Furthermore, the diversity orders achieved by both ISAC and FDSAC are identical within the same CSI case, but the OPs of FDSAC are significantly lower than those of ISAC.

In Fig. 6, we present the uplink SR as function of p_s/σ_u^2 , which verifies the analytical and approximated results. Similar to the uplink CR, while the S-C ISAC achieves the highest SR, the gap between the S-C and C-C design is negligible under the I-CSI case. It is also worth noting that regardless of

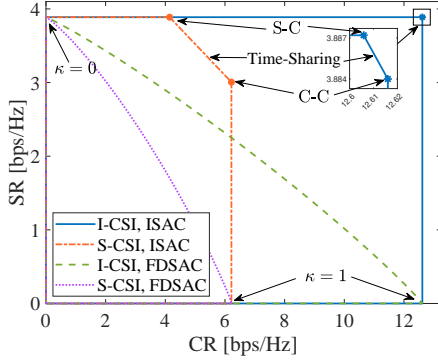


Fig. 7: Uplink rate regions with $p_c/\sigma_u^2 = p_s/\sigma_u^2 = 30$ dB.

the SIC order, ISAC is capable of achieving higher high-SNR slopes than FDSAC, which is consistent with the statements in **Remark 19**. Moving to Fig 7, we present the SR-CR regions attained by the uplink near-field FDSAC and ISAC systems with both I-CSI and S-CSI. For the region of ISAC under either I-CSI or S-CSI case, the two points on the plot correspond to the rate pairs achieved by the S-C and C-C designs, respectively, while the line segment connecting these points represents the rates attainable through the time-sharing strategy between the two designs. A pivotal observation from the plot is that the rate region of uplink FDSAC is entirely encompassed within the rate region of uplink ISAC. This unequivocally demonstrates the superior performance of ISAC over FDSAC in the uplink scenario.

VI. CONCLUSION

This paper has provided a comprehensive performance analysis of a near-field HISAC system for both downlink and uplink scenarios, where EM waves are modeled as spherical waves. To account for the closed antenna space of the holographic array, we considered the communication channels in a scattering environment as spatially correlated Rayleigh fading. Leveraging both I-CSI and S-CSI, we derived closed-form expressions and high-SNR approximations for the SRs, CRs, and OPs under the S-C and C-C designs. Furthermore, we identified the Pareto boundary of the downlink SR-CR region and characterized the uplink rate region using the time-sharing strategy. The high-SNR slopes and diversity orders of the proposed HISAC system and the baseline FDSAC system were obtained, providing further insights into system performance. The results have demonstrated that HISAC is able to achieve more DoFs and broader rate regions than the conventional FDSAC in both downlink and uplink cases, underscoring the significant performance advantages offered by the near-field HISAC system.

APPENDIX

A. Proof of Lemma 1

Vectorizing the echo signal \mathbf{Y}_s yields

$$\text{vec}(\mathbf{Y}_s) = \sqrt{p}\mathbf{h}_s^H \mathbf{w} \text{vec}(\mathbf{h}_s \mathbf{s}^H) \beta + \text{vec}(\mathbf{N}_s). \quad (\text{A.1})$$

It is important to highlight that the conditional MI between $\text{vec}(\mathbf{Y}_s)$ and β is equivalent to the capacity of a multiple-input single-output (MISO) Gaussian channel with a Gaussian

distributed input $\beta \sim \mathcal{CN}(0, \alpha_s)$: $\dot{\mathbf{y}} = \dot{\mathbf{h}}\beta + \dot{\mathbf{n}}$, where $\dot{\mathbf{h}} = \sqrt{p}\mathbf{h}_s^H \mathbf{w} \text{vec}(\mathbf{h}_s \mathbf{s}^H)$ denotes the channel vector, and $\dot{\mathbf{n}} \sim \mathcal{CN}(0, \sigma_s^2 \mathbf{I})$. Consequently, the sensing MI can be expressed as $I(\mathbf{Y}_s; \beta | \mathbf{X}) = \log_2 \det(\mathbf{I} + \dot{\mathbf{h}}\dot{\mathbf{h}}^H / \sigma_s^2)$. With the aid of Sylvester's identity, we have

$$I(\mathbf{Y}_s; \beta | \mathbf{X}) = \log_2(1 + \dot{\mathbf{h}}^H \dot{\mathbf{h}} / \sigma_s^2) \quad (\text{A.2})$$

$$= \log_2(1 + p/\sigma_s^2 L \alpha_s \|\mathbf{h}_s\|^2 |\mathbf{w}^H \mathbf{h}_s|^2). \quad (\text{A.3})$$

Substituting (A.3) into (7), we obtain the results in Lemma 1.

B. Proof of Theorem 2 and 3

Notably, the communication channel can be written as $\mathbf{h}_c = \mathbf{R}^{\frac{1}{2}} \tilde{\mathbf{h}}$ with $\tilde{\mathbf{h}} \sim \mathcal{CN}(0, \mathbf{I}_N)$. Since \mathbf{h}_s is irrelevant to \mathbf{h}_c , we have $\mathbf{h}_s^H \mathbf{h}_c = \mathbf{h}_s^H \mathbf{R}^{\frac{1}{2}} \tilde{\mathbf{h}} \sim \mathcal{CN}(0, \mathbf{h}_s^H \mathbf{R} \mathbf{h}_s)$. Hence, $|\mathbf{h}_s^H \mathbf{h}_c|^2$ is exponentially distributed with its probability density function (PDF) given by $\frac{1}{\mathbf{h}_s^H \mathbf{R} \mathbf{h}_s} e^{-\frac{x}{\mathbf{h}_s^H \mathbf{R} \mathbf{h}_s}}$. Consequently, based on (23), the ECR can be calculated as follows:

$$\mathcal{R}_{d,c}^s = \frac{1}{\mathbf{h}_s^H \mathbf{R} \mathbf{h}_s \ln 2} \int_0^\infty \ln(1 + p/\sigma_c^2 \|\mathbf{h}_s\|^{-2} x) e^{-\frac{x}{\mathbf{h}_s^H \mathbf{R} \mathbf{h}_s}} dx. \quad (\text{B.1})$$

With the aid of [29, (4.337.2)], the results in (24) can be derived.

When $p \rightarrow \infty$, by applying the fact of $\lim_{x \rightarrow \infty} \log_2(1 + x) \approx \log_2 x$, we have

$$\mathcal{R}_{d,c}^s \approx \frac{1}{\mathbf{h}_s^H \mathbf{R} \mathbf{h}_s \ln 2} \int_0^\infty \ln(p/\sigma_c^2 \|\mathbf{h}_s\|^{-2} x) e^{-\frac{x}{\mathbf{h}_s^H \mathbf{R} \mathbf{h}_s}} dx. \quad (\text{B.2})$$

With the aid of [29, (4.331.1)], we can obtain (25).

By substituting (23) into (26), the OP can be obtained as follows:

$$\begin{aligned} \mathcal{P}_d^s &= \Pr(|\mathbf{h}_s^H \mathbf{h}_c|^2 < \sigma_c^2 \|\mathbf{h}_s\|^2 (2^{\mathcal{R}_t} - 1) / p) \\ &= F_{|\mathbf{h}_s^H \mathbf{h}_c|^2}(\sigma_c^2 \|\mathbf{h}_s\|^2 (2^{\mathcal{R}_t} - 1) / p), \end{aligned} \quad (\text{B.3})$$

where $F_{|\mathbf{h}_s^H \mathbf{h}_c|^2}(x) = 1 - e^{-\frac{x}{\mathbf{h}_s^H \mathbf{R} \mathbf{h}_s}}$ represents the cumulative distribution function (CDF) of $|\mathbf{h}_s^H \mathbf{h}_c|^2$ following an exponential distribution. The high-SNR approximation can be easily obtained by applying $\lim_{x \rightarrow 0} \exp(-x) = 1 - x$ [29, (1.211.1)].

C. Proof of Theorems 4 and 5

Based on (13), by defining $\bar{\mathbf{h}} \triangleq [h_1, \dots, h_n]^H$, the communication channel gain $\|\mathbf{h}_c\|^2$ can be expressed as follows:

$$\|\mathbf{h}_c\|^2 = \bar{\mathbf{h}}^H \Sigma \bar{\mathbf{h}} = \sum_{n=1}^n \lambda_n |h_n|^2, \quad (\text{C.1})$$

Note that $\{h_n\}_{n=1, \dots, n}$ contains n independent complex Gaussian variables with $h_n \sim \mathcal{CN}(0, 1)$. Therefore, the PDF of $\sum_{n=1}^n \lambda_n |h_n|^2$, which is the sum of n independent exponentially distributed variables, is given by [30]

$$f_{\|\mathbf{h}_c\|^2}(x) = \frac{\lambda_n^n}{\prod_{n=1}^n \lambda_n} \sum_{k=0}^{\infty} \frac{\delta_k x^{n+k-1}}{\lambda_n^{n+k} (n+k)!} e^{-\frac{x}{\lambda_n}}. \quad (\text{C.2})$$

With the aid of [29, (3.351.1)], we can calculate the CDF of $\|\mathbf{h}_c\|^2$ as

$$F_{\|\mathbf{h}_c\|^2}(x) = \frac{\lambda_n^n}{\prod_{n=1}^n \lambda_n} \sum_{k=0}^{\infty} \frac{\delta_k \Upsilon(n+k, \frac{x}{\lambda_n})}{(n+k-1)!}. \quad (\text{C.3})$$

Subsequently, the OP is given by

$$\mathcal{P}_d^c = \Pr\left(\|\mathbf{h}_c\|^2 < \frac{2^{\mathcal{R}_0} - 1}{p/\sigma_c^2}\right) = F_{\|\mathbf{h}_c\|^2}\left(\frac{2^{\mathcal{R}_0} - 1}{p/\sigma_c^2}\right). \quad (\text{C.4})$$

When $p \rightarrow \infty$, by utilizing the asymptotic property of the lower incomplete gamma function [29, (8.354.1)], i.e., $\lim_{x \rightarrow \infty} \Upsilon(s, x) \simeq \frac{x^s}{s}$, within (32), we can obtain (33). Moreover, the ECR can be calculated as

$$\mathcal{R}_{d,c}^c = \int_0^\infty \log_2(1 + p/\sigma_c^2 x) f_{\|\mathbf{h}_c\|^2}(x) dx. \quad (\text{C.5})$$

With the aid of [29, (4.337.5)], we can obtain (35). When $p \rightarrow \infty$, by leveraging $\lim_{x \rightarrow \infty} \log_2(1 + x) \simeq \log_2 x$ and [29, (4.352.1)], the high-SNR approximation can be derived.

D. Proof of Theorem 6

By performing some manipulations based on (37), the average SR can be written as

$$\mathcal{R}_{d,s}^c = \mathbb{E}\{\overline{\mathcal{R}}_{d,s}^c\} = \frac{1}{L} \left(\underbrace{\mathbb{E}\{\log_2(\tilde{\mathbf{h}}^H \mathbf{\Delta} \tilde{\mathbf{h}})\}}_{P_1} - \underbrace{\mathbb{E}\{\log_2(\|\mathbf{h}_c\|^2)\}}_{P_2} \right), \quad (\text{D.1})$$

Upon applying ED to $\mathbf{\Delta}$, i.e., $\mathbf{\Delta} = \mathbf{Q} \mathbf{\Lambda} \mathbf{Q}^H$, where \mathbf{Q} is unitary and $\mathbf{\Lambda} = \text{diag}\{\lambda_{\Delta,1}, \dots, \lambda_{\Delta,t}, 0, \dots, 0\}$ with $t = \text{rank}(\mathbf{\Delta})$, and defining $\mathbf{Q}^H \tilde{\mathbf{h}} \triangleq [z_1, \dots, z_N]^H$, where $\{z_n\}_{n=1,\dots,N}$ contains N independent complex Gaussian variables with $z_n \sim \mathcal{CN}(0, 1)$, we can rewrite P_1 as follows:

$$P_1 = \mathbb{E}\{\log_2(\tilde{\mathbf{h}}^H \mathbf{Q} \mathbf{\Lambda} \mathbf{Q}^H \tilde{\mathbf{h}})\} = \mathbb{E}\left\{\log_2\left(\sum_{t=1}^t \lambda_{\Delta,t} |z_t|^2\right)\right\}, \quad (\text{D.2})$$

Consequently, both (D.2) and P_2 can be calculated by following the similar steps in Appendix C. When $p \rightarrow \infty$, the results of (39) can be obtained by following the similar steps of the high-SNR approximation derivation in Appendix B.

E. Proof of Theorem 7

Based on the Karush-Kuhn-Tucker conditions, we have

$$\begin{cases} \nabla(-\mathcal{R}) + \lambda \nabla(\|\mathbf{w}\|^2 - 1) + \mu_1 \nabla f_1 + \mu_2 \nabla f_2 = \mathbf{0}, & (\text{E.1}) \\ \mu_1 f_1 = 0, \mu_2 f_2 = 0, \mu_1 \geq 0, \mu_2 \geq 0, & (\text{E.2}) \end{cases}$$

where $f_1 = 2^{(1-\tau)\mathcal{R}} - 1 - |\mathbf{w}^H \mathbf{h}_1|^2$, $f_2 = 2^{\tau L \mathcal{R}} - 1 - |\mathbf{w}^H \mathbf{h}_2|^2$, and λ, μ_1, μ_2 are real Lagrangian multipliers. Based on (E.1), we obtain

$$\begin{cases} \mu_1 \mathbf{h}_1 \mathbf{h}_1^H \mathbf{w} + \mu_2 \mathbf{h}_2 \mathbf{h}_2^H \mathbf{w} = \lambda \mathbf{w}, & (\text{E.3}) \end{cases}$$

$$\begin{cases} \mu_1 |\mathbf{w}^H \mathbf{h}_1|^2 + \mu_2 |\mathbf{w}^H \mathbf{h}_2|^2 = \lambda \mathbf{w}^H \mathbf{w} = \lambda, & (\text{E.4}) \end{cases}$$

$$\begin{cases} \mu_1 2^{(1-\tau)\mathcal{R}} (1 - \tau) \ln 2 + \mu_2 2^{\tau L \mathcal{R}} \tau L \ln 2 = 1. & (\text{E.5}) \end{cases}$$

It can be concluded from (E.5) that μ_1 and μ_2 cannot be 0 at the same time. Therefore, we discuss three cases as follows.

Case 1: $\mu_1 > 0$ and $\mu_2 = 0$: In this case, we have

$$\begin{cases} \mu_1 \mathbf{h}_1 \mathbf{h}_1^H \mathbf{w} = \lambda \mathbf{w}, & (\text{E.6}) \end{cases}$$

$$\begin{cases} \mu_1 |\mathbf{w}^H \mathbf{h}_1|^2 = \lambda, & (\text{E.7}) \end{cases}$$

$$\begin{cases} \mu_1 2^{(1-\tau)\mathcal{R}} (1 - \tau) \ln 2 = 1, & (\text{E.8}) \end{cases}$$

$$\begin{cases} f_2 = 0 \Rightarrow |\mathbf{w}^H \mathbf{h}_1|^2 = 2^{(1-\tau)\mathcal{R}} - 1. & (\text{E.9}) \end{cases}$$

Based on the above conditions, the optimal value of \mathcal{R} and \mathbf{w} are given by $\mathcal{R}^* = \frac{1}{1-\tau} \log(1 + \|\mathbf{h}_1\|^2) = \frac{\mathcal{R}_{d,c}^c}{1-\tau}$ and $\mathbf{w}_\tau = \mathbf{h}_c \|\mathbf{h}_c\|^{-1}$, respectively. Accordingly, the SR satisfies $\overline{\mathcal{R}}_{d,s}^c \geq \tau \mathcal{R}^*$, which yields $\tau \in [0, \overline{\mathcal{R}}_{d,s}^c / (\mathcal{R}_{d,c}^c + \overline{\mathcal{R}}_{d,s}^c)]$.

Case 2: $\mu_1 = 0$ and $\mu_2 > 0$: Similar to Case 1, we can obtain $\mathcal{R}^* = \frac{\mathcal{R}_{d,s}^c}{\tau}$ and $\mathbf{w}_\tau = \mathbf{h}_s \|\mathbf{h}_s\|^{-1}$ for $\tau \in [\mathcal{R}_{d,s}^c / (\mathcal{R}_{d,c}^c + \mathcal{R}_{d,s}^c), 1]$.

Case 3: $\mu_1 > 0$ and $\mu_2 > 0$: In this case, we have $f_1 = 0 \Rightarrow |\mathbf{w}^H \mathbf{h}_1|^2 = 2^{(1-\tau)\mathcal{R}} - 1$ and $f_2 = 0 \Rightarrow |\mathbf{w}^H \mathbf{h}_2|^2 = 2^{\tau L \mathcal{R}} - 1$. From (E.3), we have $\mathbf{w} = \frac{\mu_1 \mathbf{h}_1^H \mathbf{w}}{\lambda} \mathbf{h}_1 + \frac{\mu_2 \mathbf{h}_2^H \mathbf{w}}{\lambda} \mathbf{h}_2 \triangleq a \mathbf{h}_1 + b \mathbf{h}_2$, which further yields

$$\mu_1 (\|\mathbf{h}_1\|^2 + b/a\rho) = \mu_2 (\|\mathbf{h}_2\|^2 + a/b\rho^*) = \lambda, \quad (\text{E.10})$$

where $\frac{a}{b} = \frac{\mu_1 \mathbf{h}_1^H \mathbf{w}}{\mu_2 \mathbf{h}_2^H \mathbf{w}} = \frac{\mu_1 \sqrt{2^{(1-\tau)\mathcal{R}} - 1}}{\mu_2 \sqrt{2^{\tau L \mathcal{R}} - 1} e^{-j\angle \rho}}$. By combining (E.10) and (E.5), we can derive $\mu_1 = \frac{\xi_1}{\lambda}$, $\mu_2 = \frac{\xi_2}{\lambda}$, and $\lambda = \frac{\|\mathbf{h}_1\|^2 \|\mathbf{h}_2\|^2 - \rho^2}{\lambda}$. Additionally, upon substituting the above results of μ_1, μ_2 and λ into (E.4), we obtain an equation for \mathcal{R} as follows:

$$\xi_1 (2^{\tau L \mathcal{R}} - 1) + \xi_2 (2^{(1-\tau)\mathcal{R}} - 1) = \|\mathbf{h}_1\|^2 \|\mathbf{h}_2\|^2 - \rho^2. \quad (\text{E.11})$$

Since $\xi_1 (2^{\tau L \mathcal{R}} - 1) + \xi_2 (2^{(1-\tau)\mathcal{R}} - 1)$ is a monotonic function with respect to \mathcal{R} , ranging from 0 to ∞ , the optimal solution $\mathcal{R} = \mathcal{R}^*$ can be obtained by solving (E.11). The final results can be obtained directly.

F. Proof of Corollary 1

The SR-CR regions achieved by \mathbf{w}_τ and \mathbf{w}_ς are given by

$$\mathcal{C}_\tau = \{(\mathcal{R}_s, \mathcal{R}_c) \mid \mathcal{R}_s \in [0, \mathcal{R}_s^\tau], \mathcal{R}_c \in [0, \mathcal{R}_c^\tau], \tau \in [0, 1]\},$$

$$\mathcal{C}_\varsigma = \{(\mathcal{R}_s, \mathcal{R}_c) \mid \mathcal{R}_s \in [0, \mathcal{R}_s^\varsigma], \mathcal{R}_c \in [0, \mathcal{R}_c^\varsigma], \varsigma \in [0, 1]\},$$

respectively, where $(\mathcal{R}_s^\tau, \mathcal{R}_c^\tau)$ and $(\mathcal{R}_s^\varsigma, \mathcal{R}_c^\varsigma)$ represent the rate pairs achieved by \mathbf{w}_τ and \mathbf{w}_ς , respectively. As \mathcal{C}_τ encompasses all achievable rate pairs, we have $\mathcal{C}_\varsigma \subseteq \mathcal{C}_\tau$. Moreover, since \mathbf{w}_τ is the linear combination of \mathbf{h}_c and $\mathbf{h}_s e^{-j\angle \rho}$ with non-negative real coefficients, and \mathbf{w}_ς can represent any arbitrary linear combination of \mathbf{h}_c and $\mathbf{h}_s e^{-j\angle \rho}$ with non-negative real coefficients, we have $\mathcal{C}_\tau \subseteq \mathcal{C}_\varsigma$. Therefore, we obtain $\mathcal{C}_\tau = \mathcal{C}_\varsigma$. The final results follow immediately.

G. Proof of Lemma 2

As BS does not know \mathbf{h}_c , the C-C design of \mathbf{w} is irrelevant to \mathbf{h}_c , which yields $\mathbf{w}^H \mathbf{h}_c = \mathbf{w}^H \mathbf{R}^{\frac{1}{2}} \tilde{\mathbf{h}} \sim \mathcal{CN}(0, \mathbf{w}^H \mathbf{R} \mathbf{w})$. Hence, $|\mathbf{w}^H \mathbf{h}_c|^2$ is exponentially distributed with its PDF given by $\frac{1}{\mathbf{w}^H \mathbf{R} \mathbf{w}} e^{-\frac{x}{\mathbf{w}^H \mathbf{R} \mathbf{w}}}$. Consequently, the ECR in (45) can be expressed as follows:

$$\mathbb{E}\{\overline{\mathcal{R}}_{d,c}\} = \int_0^\infty \log_2(1 + p/\sigma_c^2 x) \frac{1}{\mathbf{w}^H \mathbf{R} \mathbf{w}} e^{-\frac{x}{\mathbf{w}^H \mathbf{R} \mathbf{w}}} dx \quad (\text{G.1})$$

$$= \int_0^\infty \log_2(1 + p/\sigma_c^2 \mathbf{w}^H \mathbf{R} \mathbf{w} x) e^{-x} dx, \quad (\text{G.2})$$

which is monotone increasing with $\mathbf{w}^H \mathbf{R} \mathbf{w}$. Consequently, the problem in (45) is equivalent to

$$\mathbf{w} = \arg\max_{\|\mathbf{w}\|^2=1} \mathbf{w}^H \mathbf{R} \mathbf{w} = \mathbf{u}, \quad (\text{G.3})$$

where $\mathbf{u} \in \mathbb{C}^{N \times 1}$ is used to denote the principal eigenvector of \mathbf{R} . Furthermore, based on the ED of \mathbf{R} shown in (14), it is trivial that $\mathbf{u} = \mathbf{a}_*$.

H. Proof of Lemma 3

The superposed uplink S&C signal reads $\mathbf{Y} = \sqrt{p_s}\beta\mathbf{h}_s\mathbf{h}_s^H\mathbf{w}_s^H + \mathbf{Z}_c$. Vectorizing this signal yields

$$\text{vec}(\mathbf{Y}) = \sqrt{p_s}\beta\mathbf{h}_s^H\mathbf{w}_s + \mathbf{z}_c, \quad (\text{H.1})$$

where $\mathbf{h}_v = \text{vec}(\mathbf{h}_s\mathbf{h}_s^H)$ and $\mathbf{z}_c = \text{vec}(\mathbf{Z}_c)$. By treating (H.1) as a MISO channel model with Gaussian noise \mathbf{z}_c , the SR can be written as follows:

$$\bar{\mathcal{R}}_{u,s}^c = L^{-1} \log_2(1 + \alpha_s p_s |\mathbf{h}_s^H \mathbf{w}_s|^2 \mathbf{h}_v^H \mathbf{E}^{-1}\{\mathbf{z}_c \mathbf{z}_c^H\} \mathbf{h}_v). \quad (\text{H.2})$$

Recall that $\mathbf{Z}_c = \sqrt{p_c}\mathbf{h}_c\mathbf{h}_c^H + \mathbf{N}_u$, which together with the fact that $\mathbf{E}\{\mathbf{s}_c\mathbf{s}_c^H\} = \mathbf{I}$, yields $\mathbf{E}\{\mathbf{z}_c\mathbf{z}_c^H\} = \mathbf{I} \otimes (p_c\mathbf{h}_c\mathbf{h}_c^H + \sigma_u^2\mathbf{I})$. By further exploiting the fact that $L^{-1}\|\mathbf{s}_s\|^2 = 1$, we obtain

$$\mathbf{h}_v^H \mathbf{E}^{-1}\{\mathbf{z}_c\mathbf{z}_c^H\} \mathbf{h}_v = \mathbf{h}_s^H (p_c\mathbf{h}_c\mathbf{h}_c^H + \sigma_u^2\mathbf{I})^{-1} \mathbf{h}_s \|\mathbf{s}_s\|^2. \quad (\text{H.3})$$

By harnessing the Woodbury matrix identity, we have $(p_c\mathbf{h}_c\mathbf{h}_c^H + \sigma_u^2\mathbf{I})^{-1} = \frac{1}{\sigma_u^2}(\mathbf{I} - \frac{p_c}{p_c\|\mathbf{h}_c\|^2 + \sigma_u^2}\mathbf{h}_c\mathbf{h}_c^H)$. The final results follow immediately.

I. Proof of Theorem 12

To achieve the optimal SR, we have $\mathbf{w} = \mathbf{h}_s/\|\mathbf{h}_s\|^{-1}$, and thus the received signal of the BS at the ℓ th time slot reads

$$\mathbf{y}_\ell = \sqrt{p_c}\mathbf{h}_c\mathbf{s}_{c,\ell} + \underbrace{\sqrt{p_s}\beta\mathbf{h}_s\|\mathbf{h}_s\|\mathbf{s}_{s,\ell} + \mathbf{n}_{u,\ell}}_{\mathbf{z}_{s,\ell}} \quad (\text{I.1})$$

for $\ell = 1, \dots, L$, where $\mathbf{n}_{u,\ell} \sim \mathcal{CN}(\mathbf{0}, \sigma_u^2\mathbf{I})$ is the ℓ th column of \mathbf{N}_u . By treating $\mathbf{z}_{s,\ell}$ as a zero-mean Gaussian random variable, we calculate the CR as follows:

$$\bar{\mathcal{R}}_{u,c}^s = \log_2(1 + p_c\mathbf{h}_c^H \mathbf{E}\{\mathbf{z}_{s,\ell}\mathbf{z}_{s,\ell}^H\}^{-1} \mathbf{h}_c) \quad (\text{I.2})$$

with $\mathbf{E}\{\mathbf{z}_{s,\ell}\mathbf{z}_{s,\ell}^H\} = p_s\alpha_s\|\mathbf{h}_s\|^2\mathbf{h}_s\mathbf{h}_s^H + \sigma_u^2\mathbf{I}$, which is independent with the time slot. Hence, the ECR is given by $\bar{\mathcal{R}}_{u,c}^s = \mathbf{E}\{\bar{\mathcal{R}}_{u,c}^s\}$, which can be analyzed by following the similar steps presented in Appendix C.

J. Proof of Lemma 4

As \mathbf{h}_c is unknown to the BS, the design of \mathbf{v} is irrelevant to \mathbf{h}_c , which yields $\mathbf{v}^H\mathbf{h}_c = \mathbf{v}^H\mathbf{R}^{\frac{1}{2}}\tilde{\mathbf{h}} \sim \mathcal{CN}(0, \mathbf{v}^H\mathbf{R}\mathbf{v})$. Hence, $\frac{p_c|\mathbf{v}^H\mathbf{h}_c|^2}{p_s\alpha_s\|\mathbf{h}_s\|^2|\mathbf{v}^H\mathbf{h}_s|^2 + \sigma_u^2}$ is exponentially distributed. Based on the property of exponential distribution, maximizing the ECR $\mathbf{E}\{\bar{\mathcal{R}}_{u,c}^s\}$ is equivalent to maximizing the expectation of $\frac{p_c|\mathbf{v}^H\mathbf{h}_c|^2}{p_s\alpha_s\|\mathbf{h}_s\|^2|\mathbf{v}^H\mathbf{h}_s|^2 + \sigma_u^2}$, which yields

$$\mathbf{v}_\star = \underset{\|\mathbf{v}\|^2=1}{\text{argmax}} \mathbf{E} \left\{ \frac{p_c|\mathbf{v}^H\mathbf{h}_c|^2}{p_s\alpha_s\|\mathbf{h}_s\|^2|\mathbf{v}^H\mathbf{h}_s|^2 + \sigma_u^2} \right\} \quad (\text{J.1})$$

$$= \underset{\|\mathbf{v}\|^2=1}{\text{argmax}} \frac{\mathbf{v}^H\mathbf{R}\mathbf{v}}{\mathbf{v}^H(p_s/\sigma_u^2\alpha_s\|\mathbf{h}_s\|^2\mathbf{h}_s\mathbf{h}_s^H + \mathbf{I})\mathbf{v}}. \quad (\text{J.2})$$

By applying the Rayleigh quotient theorem, we can obtain the expression of \mathbf{v}_\star . Besides, it can be concluded that $\frac{\mathbf{v}_\star^H\mathbf{R}\mathbf{v}_\star}{\mathbf{v}_\star^H(p_s/\sigma_u^2\alpha_s\|\mathbf{h}_s\|^2\mathbf{h}_s\mathbf{h}_s^H + \mathbf{I})\mathbf{v}_\star} = \varkappa$, where \varkappa denotes the principal eigenvalue of $(p_s/\sigma_u^2\alpha_s\|\mathbf{h}_s\|^2\mathbf{h}_s\mathbf{h}_s^H + \mathbf{I})^{-\frac{1}{2}}\mathbf{R}(p_s/\sigma_u^2\alpha_s\|\mathbf{h}_s\|^2\mathbf{h}_s\mathbf{h}_s^H + \mathbf{I})^{-\frac{1}{2}}$.

REFERENCES

- [1] J. A. Zhang *et al.*, "An overview of signal processing techniques for joint communication and radar sensing," *IEEE J. Sel. Topics Signal Process.*, vol. 15, no. 6, pp. 1295–1315, Nov. 2021.
- [2] A. Liu *et al.*, "A survey on fundamental limits of integrated sensing and communication," *IEEE Commun. Surveys Tuts.*, vol. 24, no. 2, pp. 994–1034, Feb. 2022.
- [3] Z. Wei *et al.*, "Integrated sensing and communication signals toward 5G-A and 6G: A survey," *IEEE Internet Things J.*, vol. 10, no. 13, pp. 11 068–11 092, Jul. 2023.
- [4] C. Huang *et al.*, "Holographic MIMO surfaces for 6g wireless networks: Opportunities, challenges, and trends," *IEEE Wireless Commun.*, vol. 27, no. 5, pp. 118–125, Oct. 2020.
- [5] O. T. Demir *et al.*, "Channel modeling and channel estimation for holographic massive MIMO with planar arrays," *IEEE Wireless Commun. Lett.*, vol. 11, no. 5, pp. 997–1001, May 2022.
- [6] A. Pizzo, T. L. Marzetta, and L. Sanguinetti, "Spatially-stationary model for holographic MIMO small-scale fading," *IEEE J. Sel. Areas Commun.*, vol. 38, no. 9, pp. 1964–1979, Sep. 2020.
- [7] H. Zhang *et al.*, "Holographic integrated sensing and communications: Principles, technology, and implementation," *IEEE Commun. Mag.*, vol. 61, no. 5, pp. 83–89, May 2023.
- [8] —, "Holographic integrated sensing and communication," *IEEE J. Sel. Areas Commun.*, vol. 40, no. 7, pp. 2114–2130, Jul. 2022.
- [9] Y. Liu *et al.*, "Near-field communications: A tutorial review," *IEEE Open J. Commun. Soc.*, Early Access, Aug. 2023.
- [10] H. Zhang *et al.*, "6g wireless communications: From far-field beam steering to near-field beam focusing," *IEEE Commun. Mag.*, vol. 61, no. 4, pp. 72–77, Apr. 2023.
- [11] A. R. Chiriyath, B. Paul, G. M. Jacyna, and D. W. Bliss, "Inner bounds on performance of radar and communications co-existence," *IEEE Trans. Signal Process.*, vol. 64, no. 2, pp. 464–474, Jan. 2016.
- [12] M. Liu *et al.*, "Performance analysis and power allocation for cooperative ISAC networks," *IEEE Internet Things J.*, vol. 10, no. 7, pp. 6336–6351, Apr. 2023.
- [13] C. Ouyang, Y. Liu, and H. Yang, "Performance of downlink and uplink integrated sensing and communications (ISAC) systems," *IEEE Wireless Commun. Lett.*, vol. 11, no. 9, pp. 1850–1854, Sep. 2022.
- [14] —, "MIMO-ISAC: Performance analysis and rate region characterization," *IEEE Wireless Commun. Lett.*, vol. 12, no. 4, pp. 669–673, Apr. 2023.
- [15] J. Cong *et al.*, "Near-field integrated sensing and communication: Opportunities and challenges," arXiv preprint arXiv:2310.01342, 2023.
- [16] Z. Wang *et al.*, "Near-field integrated sensing and communications," *IEEE Commun. Lett.*, vol. 27, no. 8, pp. 2048–2052, Aug. 2023.
- [17] K. Qu, S. Guo, and N. Saeed, "Near-field integrated sensing and communication: Performance analysis and beamforming design," arXiv preprint arXiv:2308.06455, 2023.
- [18] H. Luo *et al.*, "Beam squint assisted user localization in near-field integrated sensing and communications systems," *IEEE Trans. Wireless Commun.*, pp. 1–1, Early Access, Oct. 3 2023.
- [19] B. Zhao *et al.*, "Modeling and analysis of near-field ISAC," arXiv preprint arXiv:2310.10917, 2023.
- [20] C. Ouyang, Y. Liu, H. Yang, and N. Al-Dhahir, "Integrated sensing and communications: A mutual information-based framework," *IEEE Commun. Mag.*, vol. 61, no. 5, pp. 26–32, May 2023.
- [21] A. Pizzo, L. Sanguinetti, and T. L. Marzetta, "Fourier plane-wave series expansion for holographic MIMO communications," *IEEE Trans. Wireless Commun.*, vol. 21, no. 9, pp. 6890–6905, Sep. 2022.
- [22] D. Starer and A. Nehorai, "Passive localization of near-field sources by path following," *IEEE Trans. Signal Process.*, vol. 42, no. 3, pp. 677–680, Mar. 1994.
- [23] B. Tang and J. Li, "Spectrally constrained MIMO radar waveform design based on mutual information," *IEEE Trans. Signal Process.*, vol. 67, no. 3, pp. 821–834, Feb. 2019.
- [24] R. Zhang and S. Cui, "Cooperative interference management with MISO beamforming," *IEEE Trans. Signal Process.*, vol. 58, no. 10, pp. 5450–5458, Oct. 2010.
- [25] Z.-Q. Luo *et al.*, "Semidefinite relaxation of quadratic optimization problems," *IEEE Signal Process. Mag.*, vol. 27, no. 3, pp. 20–34, May 2010.
- [26] B. Hassibi and B. Hochwald, "How much training is needed in multiple-antenna wireless links?" *IEEE Trans. Inf. Theory*, vol. 49, no. 4, pp. 951–963, Apr. 2003.
- [27] R. W. Heath Jr and A. Lozano, *Foundations of MIMO communication*. Cambridge, U.K.: Cambridge Univ. Press, 2018.
- [28] H. Lu and Y. Zeng, "Near-field modeling and performance analysis for multi-user extremely large-scale MIMO communication," *IEEE Commun. Lett.*, vol. 26, no. 2, pp. 277–281, Feb. 2022.
- [29] I. S. Gradshteyn and I. M. Ryzhik, *Table of Integrals, Series and Products*, 7th ed. New York, NY, USA: Academic Press, 2007.
- [30] P. G. Moschopoulos, "The distribution of the sum of independent gamma random variables," *Ann. Inst. Statist. Math.*, vol. 37, no. 1, pp. 541–544, 1985.